Scientific Research Publishing

International Journal of Geosciences, 2024, 15, 967-1019
https://www.scirp.org/journal/ijg
ISSN Online: 2156-8367
ISSN Print: 2156-8359

Petrogenesis and Sr, Nd and Pb Isotopic Characteristics of Early Palaeozoic Cambrian Kathalguri Granite, Mikir Hills North East (NE) India

Ashokaditya P. Dhurandhar

Orion Geohytech, Nagpur, India
Email: apdhurandhar@gmail.com

How to cite this paper: Dhurandhar, A.P. (2024) Petrogenesis and Sr, Nd and Pb Isotopic Characteristics of Early Palaeozoic Cambrian Kathalguri Granite, Mikir Hills North East (NE) India. *International Journal of Geosciences*, **15**, 967-1019.
https://doi.org/10.4236/ijg.2024.1512053

Received: October 23, 2024
Accepted: December 20, 2024
Published: December 23, 2024

Abstract

Early Palaeozoic Cambrian A-type Kathalguri Granites in the Mikir Hills of northeastern (NE) India were studied to better understand the geodynamic settings in this region. This research presents new whole-rock geochemical and Sr, Nd, Pb isotopic data for the Cambrian granites in the Kathalguri Granite in Mikir Hills. The Kathalguri Granite shows geochemical characteristics of high SiO_2, K_2O and low FeO^T, MgO, CaO, and P_2O_5 compositions. They belong to a high K Shoshonite to ultra-potassic series and display a weak metaluminous to peraluminous feature with A/CNK values of 0.83 to 1.02 with corundum and anorthite normative. FeO^T/MgO varies from 2.93 - 7.49, is moderately oxidized and belongs to magnetite series. The rocks have a high ΣREE composition of 370.80 - 1353.23 ppm (average 568.55) and are enriched in LREE with flat HREE and $(La/Yb)^N$ values of 8.10 - 18.99, and display obvious strong negative Eu anomalies. Trace elements of the studied granites are characterized by enrichment in Rb, Th, U, Pb, Hf, and Sm, and depletion of Ba, Nb, Ta, and Sr. They display geochemical features of high Zr + Y + Nb + Ce values (241 - 934 ppm) and Ga/Al ratios 2.49 - 3.01 consistent with A-Type granites. Based on particular geochemical features, such as high Rb/Nb (3.10 - 19.53) and Low Y/Nb (0.09 - 2.28), Kathalguri Granite can be further classified as an A1-type subgroup. Granites display relatively low Sr (<175 ppm) and Low Y (2.75 - 128 ppm), with lower Sr/Y ratios (0.82 - 37.82), $(Ho/Yb)^N$ ratio varying between 0.53 - 0.89 suggesting that the melts generated at greater depths (18 - 40 km), and fractionation at low pressures (<1000 MPa). The extremely negative Eu anomalies indicate the fractional crystallization of plagioclase and further imply that the melts generated at a pressure at a pressure range of 665 - 1481 MPa (average 920 MPa) where plagioclase is stable. Zircon

saturation temperature indicates the granitic melt crystallized at 720˚C - 834˚C. Higher radio-elemental contents (U, Th and K) resulted in high Heat Production (HHP) varying from 4.06 - 14.94 AμWm^{-3} and total HGU 98.96 to 214.20. Kathalguri Granite dated by Rb-Sr isotopic isochrone as 489 ± 19 Ma with an initial $^{87}Sr/^{86}Sr$ 0.7199 ± 0.0017 and MSWD of 4.1, $\varepsilon Sr_{(I)}$ varied between 161.62 - 332.08 suggests that the Kathalguri Granite have originated from partial melting of ancient, evolved continental crustal material. The Sm-Nd Systematics has given a depleted mantle model (T_{DM}) age ranging from 1733 - 2063 Ma with high negative εNd(t) values (−10.39 to −15.18) also hint at some heterogeneity or multiple source contributions in the melting process of the protolith. Xenoliths of older mafic rocks and Barapani arenites are seen within the Kathalguri Granite and are also supported by geochemical signatures of recycled crustal materials both mafic and sedimentary. It formed during the Cambrian reorganization of lithospheric plate motion related to the Pan-African-Braziliano event.

Keywords

Kathalguri Granite, Petrochemistry, Petrogenesis, Isotopic Age, Radiogenic Heat Generation, Geodynamic Evolution, Mikir Hills

1. Introduction

The Mikir hills in Assam form part of the Assam Meghalaya Plateau (AMP) and earn their reputation for having dense tropical rainforests, which render them highly inaccessible. Granitoids in the Mikir Hills magmatic province have intruded the underlying gneissic complex. The other associated rocks include gabbro, uralitized gabbro, monzogabbro, monzodiorite, quartz diorites, hybrid rocks, and bimodal volcanics. The adjacent Meghalaya Plateau contains coeval volcano-sedimentary rocks. The arrangement of these rocks in a linear band that stretches for approximately 240 km in a northeast-southwest direction was discovered by Nandi 2001, and Mallikharjuna *et al.* (2009) [1] [2]. The data on the chemical composition and isotopic characteristics of mafic intrusions in the Mikir Hills magmatic province is obtained from Dhurandhar *et al.*, 2019, and Prakash *et al.*, 2023 [3] [4] have discussed the Borjuri epidiorites. The zircon ages (LA-ICP-MS, U-Pb) of Kathalguri Granite 515.1 ± 3.3 Ma by Majumdar and Dutta (2106), Gogoi *et al.* (2019) [5] [6]. Kumar *et al.* [7] obtained a U-Pb SHRIMP zircon $^{207}Pb/^{206}Pb$ age of 528.7 ± 5.5 Ma for the Kaziranga granites and Longavalli monzogranite dated by SHRIMP U-Pb zircon 1430.4 ± 9.6 Ma. Hazarika *et al.* (2023) [8] also obtained an HR-SIMS U-Pb zircon age of 490 ± 11 Ma for the granitic rocks of the Bamuni Pluton. The current research is a result of Litho-geochemical, pedo-geochemical, and hydrogeochemical investigations by the Atomic Minerals Directorate's integrated investigations to assess the potential for uranium mineralization connected to unconformities in the Mikir hills (Dhurandhar, 2005;

Dhurandhar, 2010) [9] [10]. This study aims to analyse the pebble deformation, and the folding of Barapani arenite, and the petrochemistry and geodynamic processes that caused the formation of the Kathalguri Granite in the Mikir hills. Additionally, it seeks to update the chronostratigraphy of the AMP.

2. Regional Geology

Mikir Massif inliers of Assam is an extension of Shillong Plateau, surrounded by the present-day basins of Brahmaputra, Kopili, Dhanshiri, Surma-Barail alluvial plain. Archaean gneiss, Palaeo-Mesoproterozoic Shillong group of rocks, younger granite intrusive such as Bamuni, Kathalguri Dengasagaon and Dengaon granites, basic intrusive and Late Jurassic to Early Cretaceous ultra basic intrusive and alkaline/carbonatite complexes are the main geological domains (**Figure 1**). The basement is not exposed in the western margin of the plateau and it is down thrown block of Brahmaputra Graben System, largely covered by alluvium. In Mikir Massif, the Tyrsad and Barapani Formation rests above the basement gneisses and occupies an area of 400 sq km in Karbi-Anglong and Nagoan districts. Tyrsad Formation is represented by quartz sericite schist, ferruginous schist, garnetiferrous schist and quartzite intercalations as the main lithounits. Sub aerial volcanism was prevalent during Tyrsad sedimentation, represented by rhyolite/rhyodacite flows (sheared) exposed at Hanspani, Kalapani and Bhat Juri areas. Well-developed magnetite crystals occur in the form of dissemination, stringers and bandings. Tyrsad litho-units are exposed up to Kopali Juri and the unconformity contact is covered by alluvium, due to down slope of unconformity contact and off set nature of NW-SE faults. Barapani Formation overlies Tyrsad Formation with an angular unconformity, exposed all along the fringes of the contact and mainly consisting of conglomerate and variegated arenite and quartzite. It. The lithounits are conglomerate (oligomictic clast supported at places matrix supported), quartzite, grey, greenish white, buff, brown colored, quartz arenite, quartz wacke and siltstone. Unmetamorphosed loose friable, medium to coarse-grained arenite sequence shows cross-bedded and ripple marks structures are the characteristic feature of arenite. (**Figure 2**, **Figure 3**)

3. Local Geology and Structures

The conglomerate thickness varies from 3 to 15 m, showing consistent exposure to the unconformity. The conglomerate shows shearing effect in the form of stretched pebbles and schistose matrix (Hanspani River section). The pebbles are quartzite, vein quartz, sericite quartzite—all set in a schistose matrix. The pebble matrix ratio is variable hence at places, it is clast supported to matrix supported in nature (80:20). The contact between Tyrsad and Barapani Formation in Hanspani river section occurs at higher RL level (360 m) and it gradually slopes down and covered by alluvium (100 m) due to NW-SE fault displacement, cutting across both Tyrsad and Barapani Formation. The basin's margin is faulted and sheared at places. Further SW from Kopali Juri to Jiya Juri, over a stretch of 25 km only.

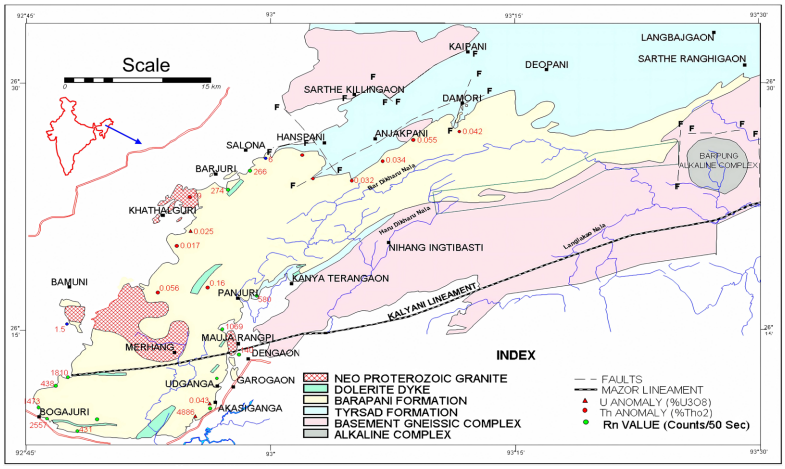

Figure 1. Regional geological map of Mikir Hills Assam also showing radon values in springs and stream's water.

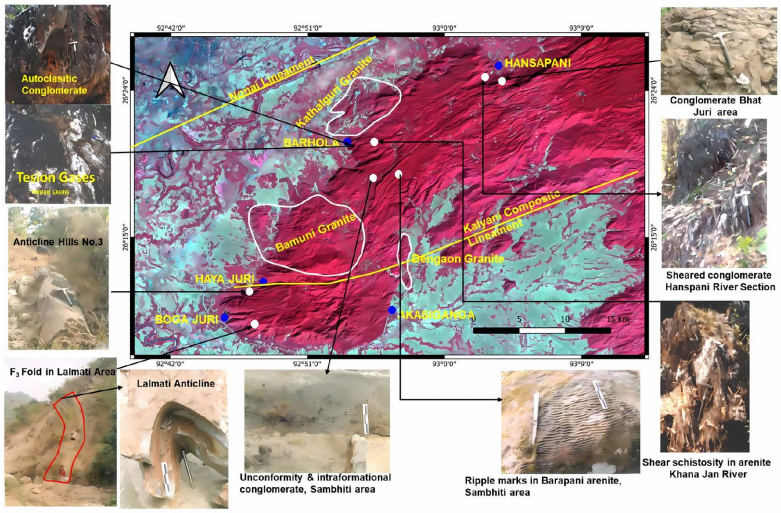

Figure 2. Photomosaic of satellite image (L9, P136 R 042, bands 543) and structural features in field photographs.

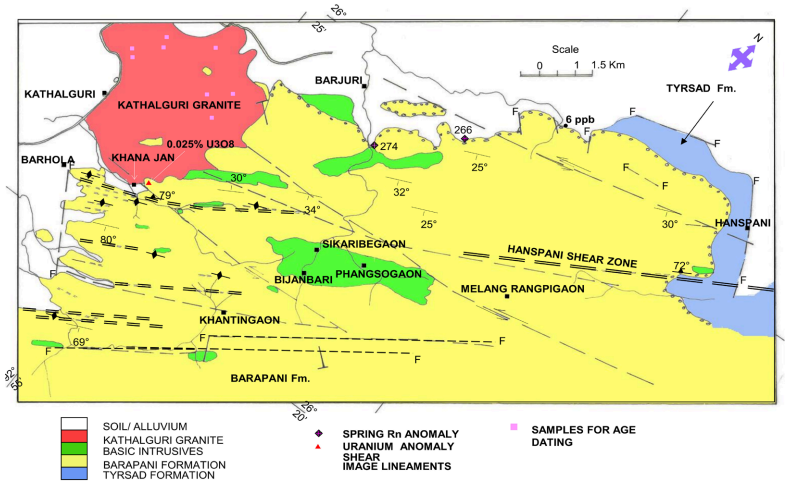

Figure 3. Geological map of the area around Kathalguri Granite Mikir Hills Assam.

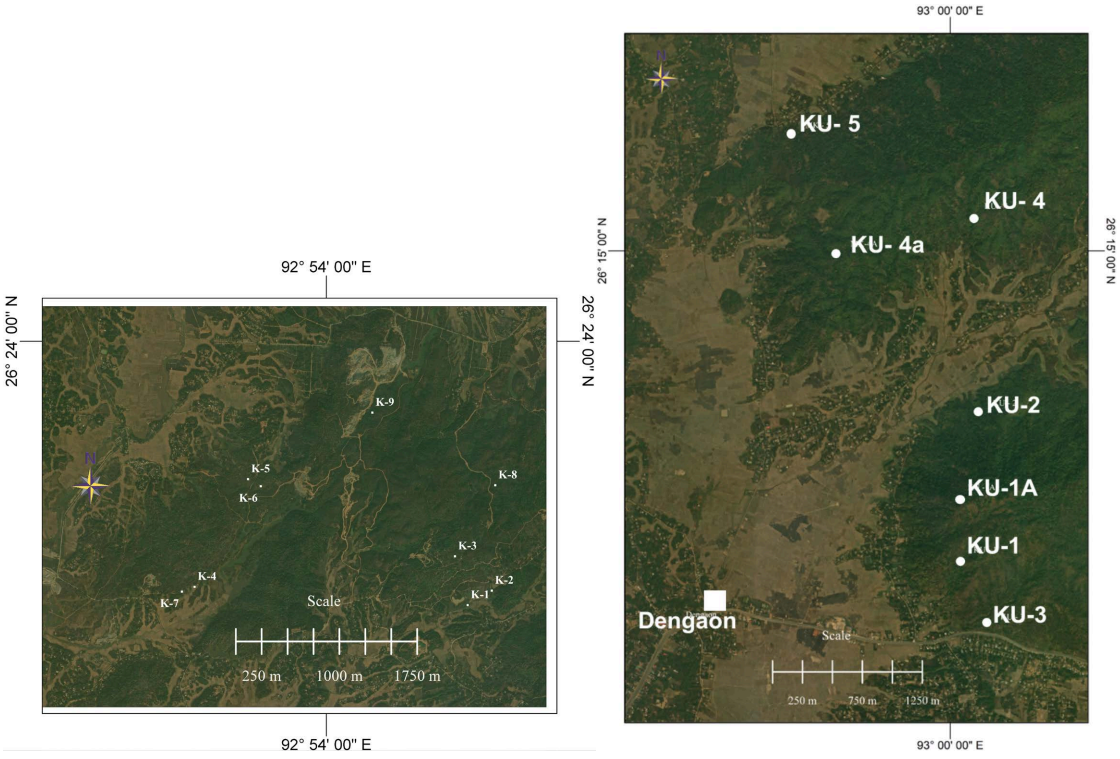

(a) (b)

Figure 4. Satellite image showing geochronological sample location, (a) Kathalguri Granite, (b) Dengaon Granite.

Barapani Formation is exposed and the unconformity contact is covered by alluvium. The thickness of cover rock varies between 100 to 600 m. The Barapani Formation contain four variants viz. lower grey quartzite of 20 - 30 m thick immediately above the conglomerate and this unit is very coarse grained, massive, hard, compact inequigranular, subangular to subrounded grey quartz rich indurated sandstone with siliceous matrix/cement. A thin layer of Pink, angular quartz grains of gritty nature occur as intercalation. It is overlained by a grey, medium-coarse grained, inequigranular, hard, compact massive sedimentary quartzite with few rounded quartz grains of pale white colour set in silicious matrix/cement with 20 - 30 m thickness (**Figure 3**). Coarse grained, equigranular, white, sub rounded to rounded quartz grains set in white silicious matrix (20 to 30 m thick) massive indurated sandstone occur further above the grey unit. Medium to coarse, white, hard compact to friable, current bedded equigranular sandstone occurs on top in Bhat Juri section at NE of Hanspani River section. In NE of Sambhiti area, along the southern side Chapanala area, a grey colour, fine grained rock with a lot of sericites is being identified as siltstone. The depositional attitude of Barapani Formation in general is NE-SW with SE dip (**Figure 1**) and the shear zone swings from vertical to subvertical due NW (Khana Jan River section 86˚, Hanspani Shear conglomerate 68˚).

The depositional attitude of Barapani Formation in general is NE-SW with SE dip (**Figure 5(a)**) and the shear zone swings from vertical to subvertical due NW (Khana Jan River section 86˚, Hanspani Shear conglomerate 68˚). The

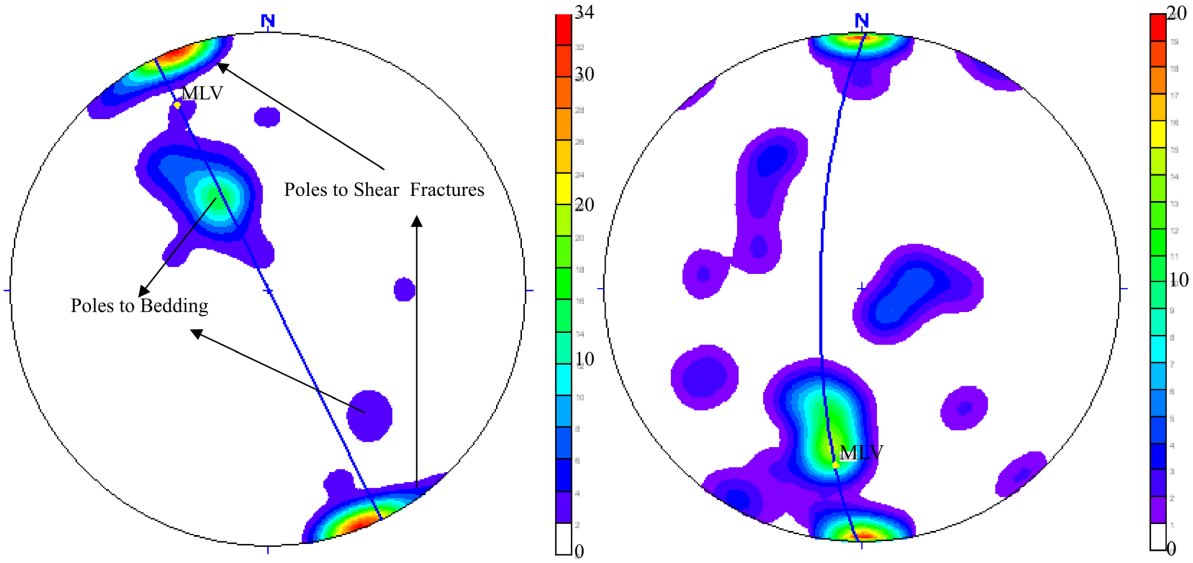

Figure 5. (a) Stereogram of bedding & shear fractures in Barapani Fm. MLV denotes mean vector lineation/value. (b) Stereogram of S0, S1 & shear fractures, MLV denotes mean vector lineation/value.

Hanspani area is traversed by a prominent N62˚E - S62˚W trending Hanspani shear zone from Barhola to Hanspani, and this shear continues further NE of Hanspani up to Damroi (**Figure 3**). This shear zone cuts across the Barapani arenaceous sequences. This shear zone can be traced in the field over 16 km strike length, and the width is about 3 km, including the sympathetic shear fractures in the studied area. The sense of shear observed in the field indicates sinistral movement. Besides, three prominent sinistral strike-slip faults have been mapped using Landsat L9 (P136 R 042) data False Color Composite 543 (**Figure 3**, **Figure 5(a)**). The analysis shows that the shear zone (Hanspani Shear) and strike-slip faults are synchronous in age as they intersect each other without any displacement (**Figure 3**, **Figure 5(a)**). The shear fractures in Barapani arenite are due to the secondary shear effect of the strike-slip fault as they make an acute angle of 30˚ with the strike-slip fault. The basic dykes have emplaced along the transpressional shears, whereas the Hanspani shear seems to be transtensional shear. Medium to coarse-grained gabbroid dykes is intrusive within the Barapani Formation, mainly confined to NE-SW deep-seated faults/transpressional shears. Gabbroid dykes are exposed at Barjuri, Phangsogaon, Bijanbari, and Hanspani river sections. The basic dykes are trending E-W and mostly cutting across both the Tyrsad and Barapani formations. The contact zone with a country rock does not show any chilling effect. The rocks are generally massive, and at places, weak schistosity has developed at the contacts. The parallelism in the trends of the bodies between themselves and with the strike of the Shillong Group appears to suggest that basic emplacement was aided by a regional tension field that led to the development of transpressional shears. The structural observations have led to deciphering the broad structural

history of the area as follows:

Folding (F1): It is represented by tight isoclinal folds with axial plane trending E-W to N60˚E - S60˚W with moderate plunge (~20˚) towards W and SW. The shape of F1 folds ranges from Class 1B to Class 1C (Based on visual observation) and its geometry is mainly upright. The banding developed due to F1 is parallel to lithological layering. Indications for F1 are well exposed at 3no. hill *colloquial as pahar* (26˚11'8"N - 92˚56'26.2"E), Samsari Juri (26˚09'40.80"N - 92˚47'18.2"E) and Boga Juri (26˚10'00"N - 92˚47'40"E).

Folding (F2): The F2 folds are open, upright isoclinal folds with axial plane trending NNE-SSW with plunge varying from 10˚ - 20˚ towards NNE to ENE. The F2 folds are coaxial to F1 and the axial plane trend varies from NNE-SSW to ENE-WSW. Indications for F2 folds are exposed at Haya Juri and Lalmati area. The shape of F2 folds tends to be Class 2 type (**Figure 5(b)**).

Folding (F3): The F1 & F2 folds are cross cut by N10˚ - 40˚W to S10˚ - 40˚E, E-W trending faults/fractures, N-S fault running along the eastern margin from Gangadisa to Panjuri via Akasiganga and the variation in the trend of axial plane of F2 may be attributed to the activity of NW-SE trending Kopilli fault.

Kathalguri Granite is grey, medium to fine grained, and equigranular hypidiomorphic granite. It is intrusive within the Barapani Formation with sharp intrusive contact exposed over an area of 30 sq.km. Pale reddish brown colour variant is also observed near the contact with quartzites of Barapani Formation.

The Shillong group of rocks are intruded by younger granites such as Bamuni, Kathalguri, and Dengaon, mostly related to Pan-African orogeny. The Kathalguri Granite has two variants, *i.e.*, Grey fine grained and Pink relatively coarse grained. The pink coarse-grained variety occurs as xenoliths within the grey variety. The Barapani arenite and quartzite also occur as xenoliths. Some of such xenoliths of very large dimensions are seen at the following locations. The Barapani arenite and quartzite also occur as xenoliths. Some of such xenoliths of very large dimensions are seen at the following locations:

1. Near Udmari village 26˚23'16.7"N - 92˚53'23.8"E strike 115˚Ndip 55˚ N10˚E friable and fine grained.
2. N. of Thekariguri 26˚22'44.5"N - 92˚54'32.8"E 20mt wide outcrop
3. Near Ranghanggaon 26˚22'03.3"N - 92˚53'22.9"E Quartzite (equivalent of Barapani) shows very prominent three sets of joints, 230˚N dip vertical, 190˚N dip 68˚ due 270˚N, 320˚N dip 70˚ due 200˚N
4. N. of Mijigaon 26˚22'26.3"N - 92˚54'12.2"E fine grained friable Barapani arenite.

Three prominent sets of joints observed are i) strike N20˚E dip 58˚ WSW, ii) strike S50˚E dip25˚ due NE, iii) strike S50˚W dip 43˚NW. The granite is also traversed by quartz veins of varying thickness and dimensions vary from a few cm to 12 inches thick. One prominent set of quartz vein strikes N40˚E and dips 47˚ NW. In general, the Kathalguri Granite shows high background radioactivity (>0.02 to 0.075mR/hr).

The basic dyke in the Bar Juri area shows sulphide mineralization, viz. pyrite,

chalcopyrite, and greenish-bluish stains of malachite and azurite. These dykes are highly jointed and appear to be sheared. The prominent sets of joints are 110˚N dip 40˚ 205˚N, N60˚E dip vertical, N20˚E dips 56˚, due 305˚N and 290˚N with sub-vertical dips. These dykes have gabbroid composition. The major litho-tectonic units in the Haya Juri-Akasiganga area (**Figure 1**) are:

1. Dongphlang anticline: fold plunges in the NE direction with the axial plane slightly curved. The core of the anticline is occupied by quartz sericite schist, Garnet-biotite schist, magnetite-bearing volcaniclastic sediments, and an E-W trending basic dyke. The southeastern limb shows dextral strike-slip, whereas the northwestern limb shows sinistral strike-slip movement.
2. Lalmati anticline: in the north of Lalmati village, the highly silicified quartzite intercalated with volcaniclastic material shows a plunging anticlinal structure. The core of the anticline is occupied by magnetite-bearing chlorite schist and volcaniclastics belonging to the Tyrsad Formation. The geometry analysis shows that this fold has an extended hinge zone and thinned limbs.
3. Barapani syncline in Rengbeng pahar, the Barapani arenite is forming syncline with plunge direction WSW. The Barapani Formation shows faulted contact with schistose and volcanoclastic of the Tyrsad Formation (**Figure 2**, **Figure 3**). The Haya Juri area (**Figure 2**) is separated by a regional lineament passing from Dobaka to Dongphlang. Towards the eastern side of this lineament, the fold patterns are completely changed, *i.e.*, they have an NNE axial plane. The sheared rhyolites are lying in the vicinity of Jhaluk Parbat. The eastern margin of Haya Juri block is also a faulted boundary, as is the southern margin. Along the southern margin, a wide basic sill has intruded the Shillong group of rocks (**Figure 2**). In the vicinity of this sill, the quartzite has become very hard, compact, and highly silicified and hence forms ridges (**Figure 2**, **Figure 3**). The radiometric and hydrogeochemical surveys have resulted in locating several uranium and thorium anomalies besides high radon anomalies associated with faults and fractures (**Figure 1**).

- The conglomerate is oligomictic ortho-conglomerate and, at places, para-conglomerate. The conglomerate is traversed by a quartz vein striking 340˚N and dipping 38˚ 260˚N. The satellite image analysis resulted in the preparation of a lithostructural map and the decipherment of regional structures. The conglomerates were analysed by tracing 125 pebbles from the X-Y and X-Z portions of the outcrop. A fry map [11] was prepared (**Figure 6**) for X-Y section (**Figure 6(a)**), and X-Z section (**Figure 6(b)**). Finite strain analysis of pebble axis (n = 125) from S of Hanspani 26˚25'08.0"N, 93˚03'04.0"E: 26˚25'06.2" N, 93˚02'59.5"E shows that the finite ellipsoid has strain shape K= 1.547079, strain intensity D = 0.883437, d = 1.1079 & lodes parameter μ = 0.2148, hence occupies the LS tectonite field in Flinn's diagram (**Figures 7-10**) [12]-[17]. The Log Flinn diagram (**Figure 8**, **Figure 9**) shows dual fabric which is common in areas subjected to transpressional tectonics, where both compressive and shear forces are at work.

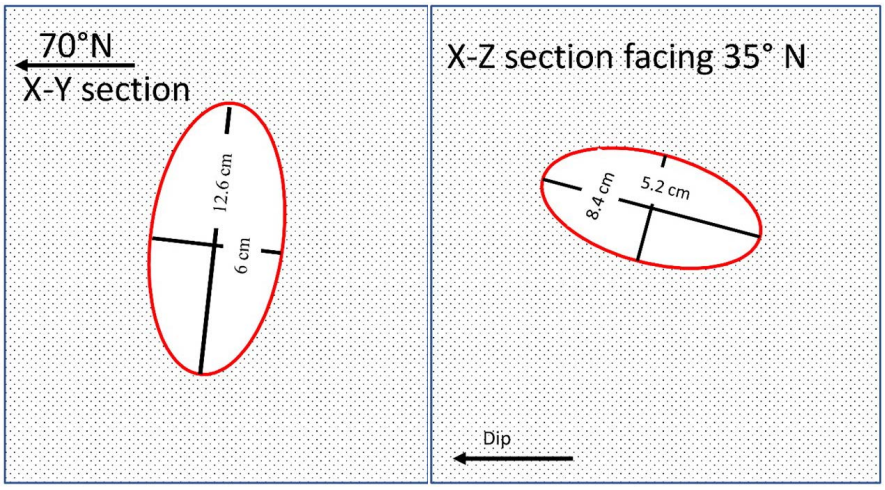

(a) (b)

Figure 6. Fry map [11] showing the finite strain ellipsoid's dimensions, (a) X-Y section, (b) X-Z section.

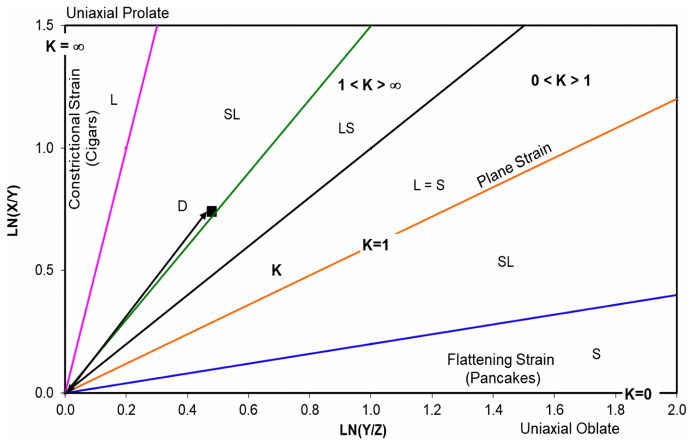

Figure 7. Ramsey and Woods plot [12] for tectonic classification of stretched pebbles of Mikir Hills Assam India. Mean K = 1.547079, D = 0.883437.

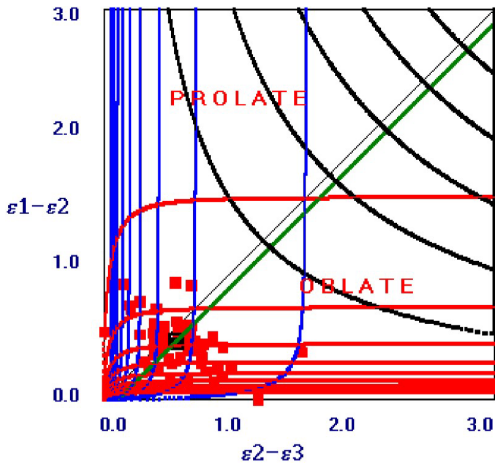

Figure 8. Logarithmic Flinn diagram for location [13] the stretched pebble mean plot at oblate field.

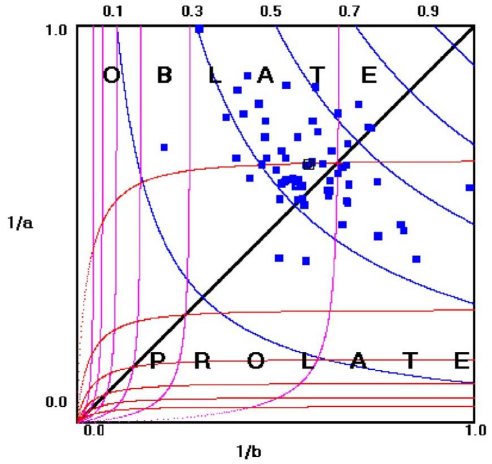

Figure 9. Logarithmic Flinn's plot for pebbles showing mean at an oblate field.

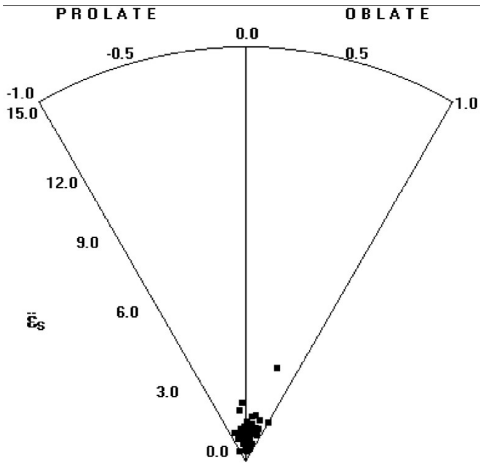

Figure 10. Hsu diagram [16] with Flinn's k-values for pebbles of Mikir Hills, represents an intermediate zone between pure flattening and pure constriction.

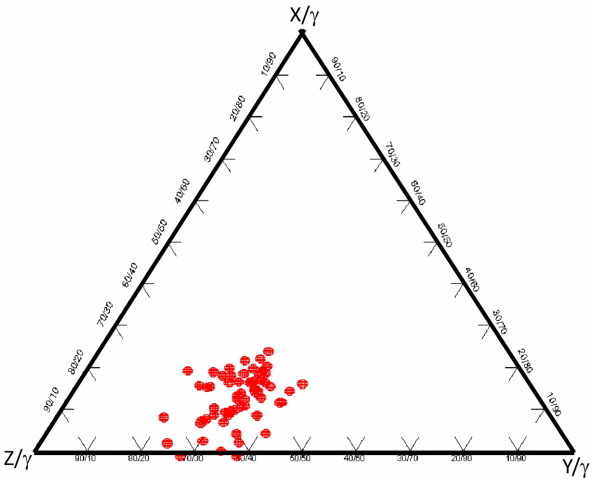

Figure 11. Burns and Spry triangular diagram (log x/γ, log y/γ, log z/γ) [17] for pebbles of Mikir hills.

This is further supported by the ternary plots of Burns and Spry 1969 [17] Log X/γ, Log Y/γ and Z/γ where $\gamma = \sqrt{(Z^*Y^*Z)}$ (**Figure 11**). The intermediate position on the Burns and Spry diagram (**Figure 11**), where the strain ratios of x, y, and z are more balanced. The intermediate position of LS tectonites on the Burns and Spry diagram suggests a strain regime influenced by both compressive and extensional forces, consistent with transpressional or transtensional settings, that typically occur in complex tectonic settings, like those near the study area, where both ancient (Brahmaputra Rifting) and younger tectonic events (Kathalguri Granite intrusion) have influenced the deformation fabric. The deformed pebbles plot in the oblate field, although it is a little away from plane straight-line occupying prolate field with constrictional nature. (Ramsay and Woods, 1973) [12]. Indicating that the conglomerate has suffered initial pre-tectonic compaction, the initial tectonic deformation increments can give rise to apparent constrictive finite strains with the X-axis at right angles to the tectonic X-axis, with a certain value of initial compaction and superposed tectonic deformation. Such type of features developed due to mixed tectonic regime in the Mikir hills as the area lies in the vicinity of Kathalguri Granite and Brahmaputra rift. The modified lithostratigraphic succession after Dhurandhar *et al.* 2019 [3] of Mikir hills is given in **Table 1**.

4. Sampling and Analytical Techniques

The representative, fresh, co-genetic, widely distributed, unweathered, and undeformed samples belonging to different suites of rocks, of approximately 10 - 12 kg of weight were collected to minimize open system behavior and local contamination. The bulk samples were cleaned, broken, and crushed in a Jaw crusher. After quartering and coning, a representative sample was ground to −200 mesh in a shatter box for whole rock isotopic analysis. One set of samples was analyzed for major, minor, and trace elements by wavelength dispersive X-ray fluorescence method using international standards as reference USGS, INRT IGI, RIAP, and namely: G1, G2, GSP1, GS-N, SG-1a, SG2, SG3. The accuracy in the analysis of relative analytical uncertainties is estimated as follows: Si, Al (<1%), Fe, Mg, Ca (1% - 2%), Ti, Na, K (3% - 5%), P, and other trace elements (≤6%). The rare earth elements were analyzed by ICP-MS at the Shiva analytical laboratory Bangalore, India. The other representative powdered samples were digested using concentrated HF and HNO_3 in Teflon digestion bombs at 130˚C for 48 hours. The dissolution followed this in HCl acid. Separation of Rb and Sr from dissolved rock solutions was carried out by ion-exchange chromatography using AG 50WX12 cation exchange resin in the clean lab under laminar flow. Quantitative estimation of these elements was done by spiking a known amount of mixed ^{87}Rb-^{84}Sr tracer before decomposition. Rb and Sr isotopic composition were analyzed following conventional mass spectrometric isotopic dilution techniques with a fully automated, multi-collector thermal ionization mass spectrometer model VG-354. Rb and Sr were loaded as chloride and nitrate on the Ta ribbon single filament beads

with 1 μL of 1N H_3PO_4. The ^{87}Rb and ^{87}Sr tracers used for determining Rb and Sr were calibrated against gravimetrically prepared solutions of J. M. (Johnson Matthey) salts. Appropriate fractionation corrections were applied to improve the accuracy. Based on the replicated analysis, the errors at the 2 level are 2% in $^{87}Rb/^{86}Sr$ and 0.05% in $^{87}Sr/^{86}Sr$. The mean value for the ($^{87}Sr/^{86}Sr$) ratio of the SRM-987 standard was 0.71024123 (N = 15). The Excel plugin Isoplot 3.7 software (Ludwig, 2012) [18] was used to calculate the slope and intercept of the isochrons. Errors in ages and initial Sr-ratios quoted here are two standard deviations. More information on the age-dating analytical processes can be found elsewhere (Pandey *et al.*, 1997) [19].

Table 1. Lithostratigraphy of Mikir Hills, Assam.

Period		Formation	Rock Type
Quaternary			Alluvium
Jurassic-Cretaceous		Intrusive	Ultrabasic (Pyroxenite), Dolerite/gabbro and Alkaline Complexes of Barpung, Jasra and Samchampi
Late Proterozoic-Early Palaeozoic (500 - 800 Ma)		Intrusive	Grey/pink hypidiomorphic granite Porphyritic granite viz. Bamuni Granite, Kathalguri Granite (489 ± 19 Ma), and Dengaon Granite (558 ± 43 Ma)
Middle Proterozoic		Intrusive	Gabbroid Dykes (1200 ± 67 Ma)
Early-Middle Proterozoic	Shillong Group	Barapani Formation (Arenaceous)	Cross-laminated/Cross-bedded gritty sandstone, Pale green-grey sandstone Buff, medium-grained, whitish brown sandstone with magnetite arenite. Grey, fine to medium-grained grey sandstone with magnetite (>560-Ma detrital zircons). Oligomictic conglomerate at the base
		Angular Unconformity	
Early Proterozoic		Tyrsad Formation (Argillaceous)	Volcanics: Rhyolite, Tuffaceous/volcanoclastics bands + magnetite Ferruginous schist Quartzite (>1100 Ma detrital zircon) and schist intercalation + magnetite
Fault contact/unconformity			
Archaean Basement Complex			Granite Gneiss, Porphyritic granite, and Migmatite (1100 to 1650 Ma based on Zircon dates)

Modified after Dhurandhar *et al.*, 2019 [3].

Table 2. Modal mineralogy on Kathalguri Granite.

Minerals	APD/K/1	APD/K/2	APD/K/3	APD/K/4	APD/K/5	APD/K/6	APD/K/7	APD/K/8	APD/K/9
Quartz	36.4	38.1	37.8	26.5	35.2	39.4	35.8	38.5	36.2
Alkali Feldspar	39.3	40	45	39.8	37.1	36.5	44.1	41.2	40.5
Plagioclase	24.3	21.9	17.1	33.7	27.7	24.1	20.1	20.3	23.3
Biotite	5.5	5.2	6.2	10.2	9.6	5	6.7	6.3	6.3

5. Petrography

The Kathalguri Granite is leucocratic; pale gray specks of biotite are visible on the surface of hand specimens. The rock is medium to fine-grained inequigranular with a hypidiomorphic texture. The essential minerals are quartz, orthoclase, microcline-microperthite, and plagioclase feldspars with accessories biotite, chlorite, sphene, zircon, apatite, and opaques. All the minerals are subhedral to partly euhedral except the quartz; the anhedral grains of quartz show undulose extinction. Microfracturing is moderate in all the grains. Orthoclase and microcline-microperthite both form subrectangular laths that show variable degrees of perthitisation. Patch micropertitisation is the most common form of alteration in all the grains of microperthite (**Figure 12(e)**). Plagioclase forms elongated laths and shows polysynthetic twinning. They are identified as albite-oligoclase (**Figure 12(b)**). Alteration to sericite is minor in two samples APD/K/3 and APD/K/4, moderate in five samples APD/K/1, APD/K/2, APD/K/3, APD/K/5, and APD/K/8 and APD/K/9 and intense in two samples APD/K/6 and APD/K/7 (**Figure 12(a)**, **Figure12(c)**, **Figure12(e)**, and **Figure12(f)**). Saussuritisation is observed in samples APD/K/2 and APD/K/8 to a moderate extent leading to the development of a fine-grained admixture of albite, epidote, calcite, and sericite. Myrmekitic intergrowths are observed at the interface of K-feldspar resulting in worm-like fine quartz grains (**Figure 12(c)**). Biotite forms a significant accessory mineral exceeding 5% in almost all the samples. Biotite commonly forms small-sized micaceous flakes, brownish yellow in color, which are chloritized to varying degrees. Only traces of cleavage surface are seen in those flakes of biotite which are almost chloritized, and the iron oxide leached out forms' streaks of magnetite. Geothetisation of magnetite leading to the formation of secondary iron oxides is also observed. Zircon is present in significant quantity as an accessory mineral forming small prismatic grains (**Figure 12(d)**). Very fine-sized zircon occurs as inclusions in biotite around which pleochroic haloes have developed in all the samples. Muscovite has developed later in many samples due to later K metasomatism, and the resultant broad flakes are conspicuous in three samples APD/K/1, APD/K/4, and APD/K/9 (**Figure 12(b)**). Allanite is another significant accessory mineral forming cubic grains flattened on 100 and small-sized laths and is seen in one sample APD/K/7. Sphene forms typical wedge-shaped grains with high relief, and its interference color is marked by the strong body color present in three samples APD/K/4, APD/K/5, and APD/K/7. Apatite is a ubiquitous accessory mineral observed in all nine samples as fine anhedral grains. Magnetite is the dominant ore mineral present as medium to coarse grains showing pale grey reflectance and is isotropic. The modal mineralogy is given in **Table 2**. It contains >5% biotite, and the rock is named Biotite granite. The QAP plot after Streckeissens 1976 [20] shows that they are granite Syeno-Granite (Three samples) to Monzo-Granite six samples (**Figure 13(a)**) equally supported by normative Or + Ab-2Q-4An ternary plot (**Figure 13(b)**, **Table 4**).

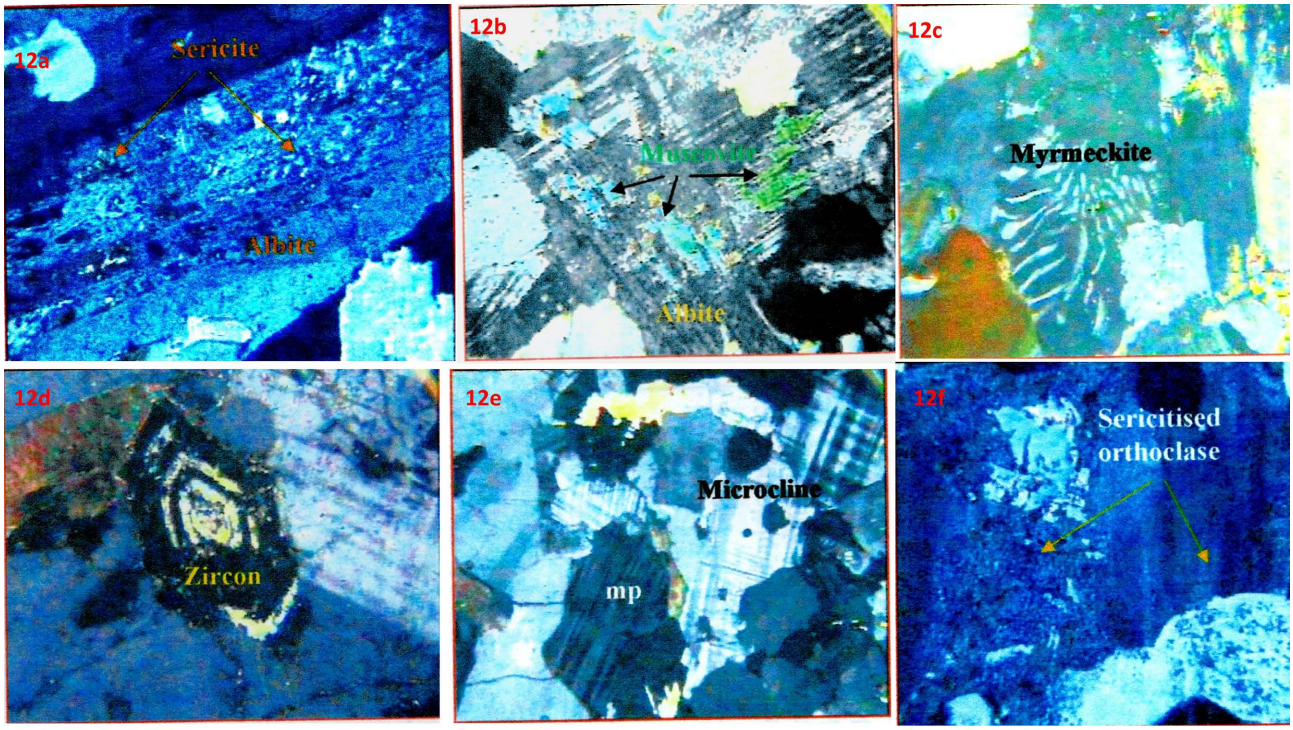

Figure 12. Microphotographs of Kathalguri Granite with X16, 2N and TL. (a) Intense alteration of plagioclase feldspar (albite) sericite (APD/K/8). (b) Muscovitisation in albite. Large flakes of Muscovite visible (APD/K/9). (c) Myrmeckite at interface of orthoclase and albite (APD/K/2). (d) Prismatic Zircon with overgrowth rings (Grain size 0.05 mm × 0.02 mm) (APD/K/1). (e) Microcline and micro perthite with minor alteration to sericite (APD/K/4). (f) Orthoclase showing high degree of alteration to sericite (APD/K/6).

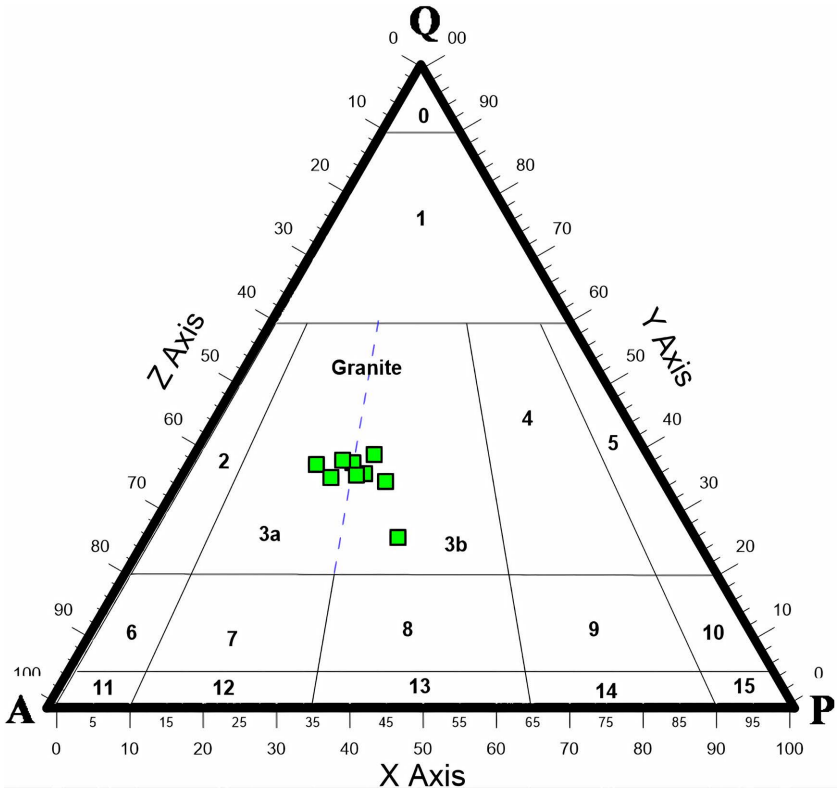

(a)

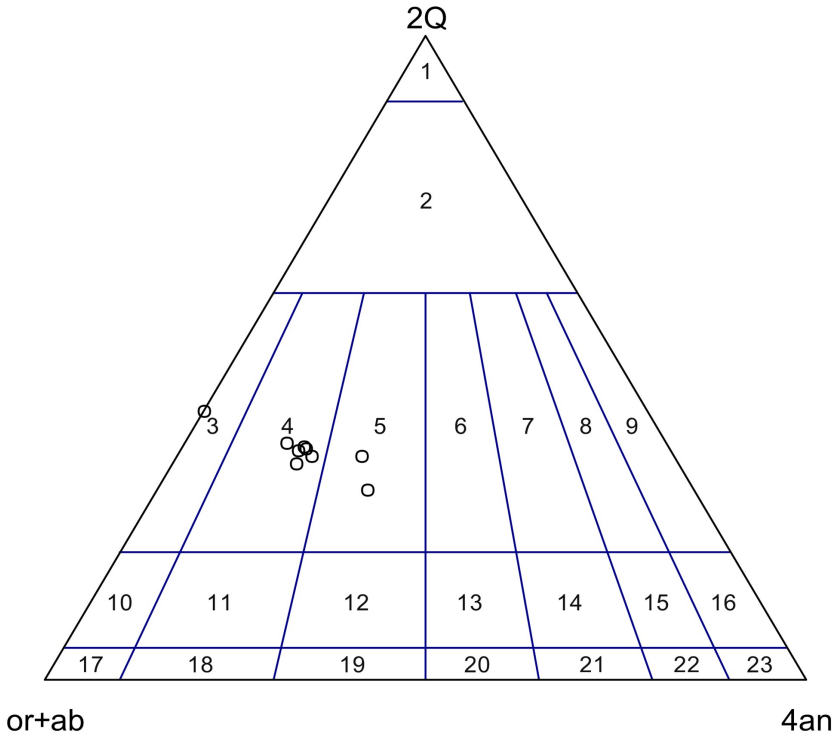

(b)

Figure 13. (a) Modal QAP Diagram after Strieckessens (1976) [20] for Kathalguri Granite. Fields. 0 Quartzolite, 1 Quartz rich Granitoid, 2 Alkali Feldspar Granite, 3a SNG Syeno-Granite, 3b MZG Monzo-Granite, 4 Granodiorite, 5 Tonalite, 6 Quartz alkali feldspar Syenite, 7 Quartz Syenite, 8 Quartz Monzonite, 9 Monzodiaorite Monzogabbro, 10 Quartz Diorite Quartz Gabbro, Quartz Anorthosite, 11 Alkali Feldsapr Syenite, 12 Syenite, 13 Monzonite, 14 Foid bearing Monzo diorite monzo gabbro, 15 Diorite, Gabbro Anorthosite. (b) Normative (Or + Ab) - 2Q - 4An Ternary plot for Kathalguri Granite occupying Syeno-Granite (n = 7) to Monzogranite Field (n = 2) after Enriques 2018 [21]. 1 quartzolite, 2 quartz-rich granitoids, 3 al kali-feldspar granite, 4 syenogranite + sub-anorthite monzogranite, 5 monzogranite, 6 granodiorite, 7 tonalite, 8 tonalgabbro, 9 tonaleu crite, 10 quartz alkali-feldspar syenite, 11 quartz syenite, 12 quartz monzonite, 13 quartz monzodiorite/quartz monzogabbro, 14 quartz diorite, 15 quartz gabbro, 16 quartz eucrite, 17 alkali feldspar syenite, 18 syenite, 19 monzonite, 20 monzodiorite/monzogabbro, 21 diorite, 22 gabbro, 23 eucrite.

6. Petrochemistry and Petrogenesis

The analytical results for whole rocks are presented in **Table 3**. They exhibit high SiO_2 (63.41 - 71.94 wt%) with an average of 69.28%, and high K_2O 5.41 - 6.27 wt.% with an average of 5.86%, moderate Al_2O_3 12.61-14.63wt.% (avg. 13.84%), low 2.28 - 3.98 wt% (avg. 3.27%) Na_2O low CaO 0.95-3.28 wt% (average 1.61%), MgO 0.35 - 2.25 wt.% (Avg. 0.81%), Fe_2O_3 0.753 - 2.307 wt.% (Avg. 1.15%), FeO 1.398 - 4.284 wt% with an average of 2.14%, and TiO_2 0.22 - 1.18 wt.% (avg. 0.44%) values. The Kathalguri Granite shows enrichment in TiO_2, Al_2O_3, FeO, Fe_2O_3, MgO, CaO, Na_2O, K_2O, P_2O_5, V, Cr, Ni, Co, Cu, Ga, As, Rb, Zr, Ba, Ce, Pb, and depletion in SiO_2, MnO, Zn, Sr, Y, Nb, Th, U as compared to normal granite of Wedepohl 1969 [22]. Kathalguri Granite shows enrichment in SiO_2, Na_2O, K_2O, P_2O_5, Ga, As, Rb,

Sr, Zr, Ba, Ce, Pb, and Depletion in TiO_2, Al_2O_3, FeO, Fe_2O_3, MgO, MnO, CaO, V, Cr, Co, Ni, Cu, Zn, Y, Nb, Th, U as compared to the continental crust Gao *et al.* 1998 [23]. On chondrite-normalized multi-element plots (**Figure 14(a)**), the Kathalguri Granite shows relative enrichments in Rb, Ba, Th, U, K, Nb, Ce, Sr, Zr, and with pronounced negative P, and Ti and Y (n = 2) anomalies (Thompson 1982) [24]. The same patterns are shown in primitive mantle normalized plots after

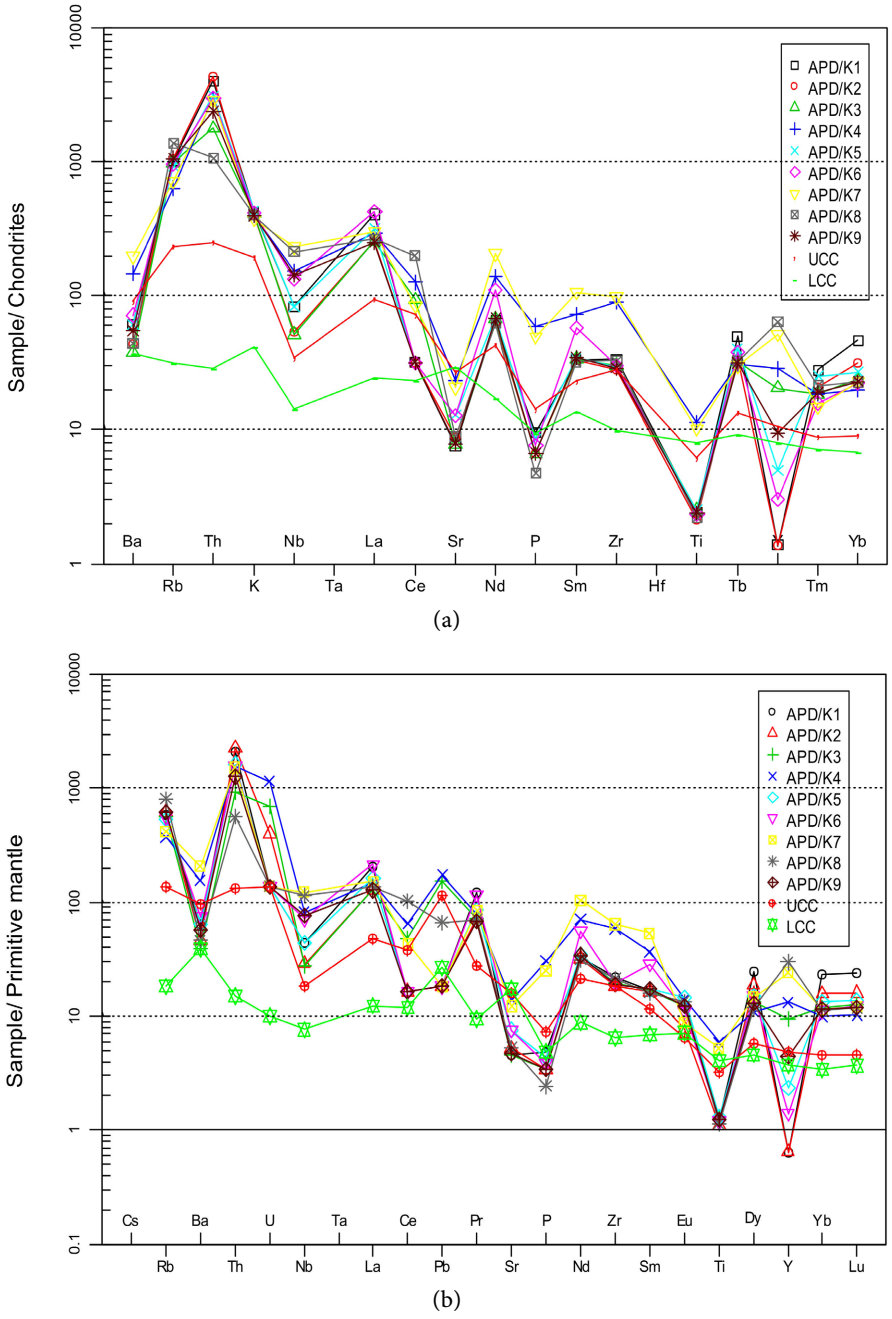

Figure 14. (a) Chondrite normalized Extended Spider plot (Thompson 1982) [24] for Kathalguri Granite. Upper Continental Crust (UCC), Lower Continental Crust (LCC). (b) Primitive mantle normalized extended spider plot after Sun and Macdonough 1989 [25] for Kathalguri Granite. Upper Continental Crust (UCC), Lower Continental Crust (LCC).

Table 3. Geochemical data on Kathalguri Granite.

Oxide/Elements	APD/K1	APD/K2	APD/K3	APD/K4	APD/K5	APD/K6	APD/K7	APD/K8	APD/K9	Min	Max	Avg	σ
SiO_2	70.53	71.1	69.86	63.42	70.82	70.15	64.98	70.73	71.94	63.42	71.94	69.28	2.97
TiO_2	0.25	0.22	0.26	1.18	0.26	0.24	1.05	0.23	0.25	0.22	1.18	0.44	0.39
Al_2O_3	14.63	14.41	14.41	13.18	14.35	14.35	12.61	14.05	12.61	12.61	14.63	13.84	0.81
FeO	1.398	1.443	1.502	4.284	1.463	1.723	3.868	1.703	1.859	1.398	4.284	2.14	1.11
Fe_2O_3	0.753	0.777	0.809	2.307	0.788	0.928	2.083	0.917	1.001	0.753	2.307	1.15	0.60
MgO	0.47	0.39	0.48	2.25	0.59	0.49	1.8	0.35	0.46	0.35	2.25	0.81	0.70
MnO	0.04	0.04	0.04	0.11	0.04	0.03	0.09	0.08	0.05	0.03	0.11	0.06	0.03
CaO	1.17	1.19	1.21	3.28	1.38	1.22	2.93	0.95	1.18	0.95	3.28	1.61	0.86
Na_2O	3.42	3.6	3.65	2.28	3.24	3.28	2.37	3.64	3.98	2.28	3.98	3.27	0.58
K_2O	6.1	5.73	5.95	5.78	6.27	6.03	5.41	5.77	5.74	5.41	6.27	5.86	0.25
P_2O_5	0.1	0.07	0.07	0.63	0.09	0.08	0.52	0.05	0.07	0.05	0.63	0.19	0.22
Sc	4.45	4.79	5.41	6.054	6.22	4.8	4.97	5.92	5.92	4.45	6.22	5.39	0.66
V	28	18	24	91	13	10	71	2.75	28	2.75	91	31.75	29.57
Cr	30	21	15	22	20	63	39	75	65	15	75	38.89	22.86
Co	6	11	2.75	13	2.75	2.75	11	10	2.75	2.75	13	6.89	4.33
Ni	21	29	18	27	18	41	31	63	56	18	63	33.78	16.35
Cu	11	15	9	10	10	15	18	13	6	6	18	11.89	3.69
Zn	48	48	45	113	31	25	98	54	49	25	113	56.78	29.36
Ga	22	19	22	21	19	20	20	20	19	19	22	20.22	1.20
As	14	5.5	11	10	5.5	5.5	11	5.5	5.5	5.5	14	8.17	3.34
Rb	354	371	345	224	324	339	251	484	373	224	484	340.56	74.70
Sr	90	104	92	278	151	150	244	105	93	90	278	145.22	70.15
Y	2.75	2.75	41	57	10	6	104	128	19	2.75	128	41.17	46.62
Zr	231	192	206	618	201	207	676	224	199	192	676	306	194.25
Nb	29	19	18	54	29	47	81	75	50	18	81	44.67	22.97
Ba	424	305	261	1021	423	497	1363	305	381	261	1363	553.33	379.09
Ce	27.5	27.5	81	109	27.5	27.5	73	173	27.5	27.5	173	63.72	51.16
Pb	2.75	2.75	23	26	2.75	2.75	2.75	10	2.75	2.75	26	8.39	9.47
Th	170	181	75	125	131	125	122	45	101	45	181	119.44	42.43
U	2.75	8	14	23	2.75	2.75	2.75	2.75	2.75	2.75	23	6.83	7.19
					Rare earth Elements								
La	134.1	83.85	84.06	97.36	104.77	138.98	98.51	87.62	82.42	82.42	138.98	101.30	21.44
Ce	27.25	175.42	166.78	181.83	198.01	274.40	205.96	163.66	160.11	27.25	274.40	172.60	64.82
Pr	31.05	18.115	18.155	19.84	21.98	29.46	21.33	17.97	17.47	17.47	31.05	21.71	5.11
Nd	41.2	40.3	42.2	88.1	43.5	70	130	39.2	42.90	39.20	130.00	59.71	31.31
Sm	6.78	6.65	6.87	14.9	6.96	11.7	21.7	6.5	7.05	6.50	21.70	9.90	5.31

Continued

Eu	1.9	1.195	1.875	2.175	2.245	1.71	1.35	2.065	1.91	1.20	2.25	1.83	0.35
Gd	16.75	10.44	11.40	12.23	14.89	15.39	10.85	12.17	11.34	10.44	16.75	12.83	2.26
Tb	2.6	1.745	1.665	1.615	2.1	1.97	1.57	1.69	1.64	1.57	2.60	1.84	0.33
Dy	16.75	12.55	9.125	7.42	10.035	10.095	9.815	8.14	8.71	7.42	16.75	10.29	2.83
Ho	1.85	1.4	1.325	1.345	1.855	1.215	1.055	1.5	1.37	1.06	1.86	1.44	0.27
Er	6.7	4.965	4.39	4.28	5.84	4.12	3.68	4.81	4.46	3.68	6.70	4.81	0.93
Tm	0.95	0.695	0.625	0.63	0.855	0.535	0.495	0.73	0.65	0.50	0.95	0.69	0.14
Yb	10.25	6.975	5.225	4.38	5.94	4.935	5.04	5.02	5.04	4.38	10.25	5.87	1.80
Lu	1.65	1.085	0.85	0.7	0.94	0.835	0.815	0.8	0.81	0.70	1.65	0.94	0.29
Y	54	87	41	57	10	6	104	128	19.00	6.00	128.00	56.22	42.81
Eu/Eu*	0.544	0.438	0.647	0.492	0.674	0.389	0.269	0.709	0.652	0.269	0.709	0.535	0.150
(La/Yb)N	8.9	8.18	10.95	15.13	12	19.17	13.3	11.88	11.13	8.18	19.17	12.44	3.52
ΣREE	358.23	457.18	400.95	499.85	436.14	576.14	621.13	485.80	370.80	358.23	621.13	467.36	89.16
ΣLREE	246.73	330.32	325.35	410.26	383.69	531.04	483.82	322.94	317.77	246.73	531.04	372.43	89.69
ΣHREE	111.50	126.86	75.60	89.60	52.45	45.10	137.32	162.86	53.02	45.10	162.86	94.92	42.06
Critical Ratios and Critical Indices													
Na_2O+K_2O	0.56	0.63	0.61	0.39	0.52	0.54	0.44	0.63	0.69	0.39	0.69	0.56	0.10
Mol A/CNK	1.02	1.01	0.98	0.83	0.98	1.01	0.84	1.01	0.85	0.83	1.02	0.95	0.08
Mol A/NK	1.20	1.19	1.16	1.32	1.18	1.20	1.29	1.15	0.99	0.99	1.32	1.19	0.09
Na_2O/Al_2O_3	0.23	0.25	0.25	0.17	0.23	0.23	0.19	0.26	0.32	0.17	0.32	0.24	0.04
K_2O/Al_2O_3	0.42	0.40	0.41	0.44	0.44	0.42	0.43	0.41	0.46	0.40	0.46	0.42	0.02
$FeO^{(T)}/MgO$	4.57	5.69	4.81	2.93	3.81	5.41	3.31	7.49	6.22	2.93	7.49	4.92	1.46
SI	9.11	9.34	9.22	18.29	10.50	9.26	17.59	7.32	8.58	7.32	18.29	11.02	4.01
LI	25.82	25.63	25.24	14.80	25.66	25.05	16.39	25.43	25.22	14.80	25.82	23.25	4.36
DI	89.68	90.01	89.17	75.49	89.31	88.59	77.27	90.11	92.16	75.49	92.16	86.86	6.04
FI	89.06	88.69	88.81	71.08	87.33	88.41	72.64	90.83	89.17	71.08	90.83	85.11	7.58
R1	2051	2112	1960	2034	2094	2092	2195	2064	2030	1960	2195	2070	65
R2	435	429	436	721	458	436	650	395	396	395	721	484	117
Colour Index	3.29	3.21	3.56	13.12	3.69	3.82	11.47	3.65	5.55	3.21	13.12	5.71	3.82
Agpaitic Index	0.84	0.84	0.86	0.76	0.84	0.83	0.77	0.87	1.01	0.76	1.01	0.85	0.07
HPU	12.82	14.94	9.09	14.92	10.09	9.67	9.43	4.06	7.98	4.06	14.94	10.33	3.47
K/Rb	143.04	128.21	143.16	214.20	160.64	147.65	178.92	98.96	127.74	98.96	214.20	149.17	33.05
Rb/Zr	1.53	1.93	1.67	0.36	1.61	1.64	0.37	2.16	1.87	0.36	2.16	1.46	0.65
Rb/Sr	3.93	3.57	3.75	0.81	2.15	2.26	1.03	4.61	4.01	0.81	4.61	2.90	1.38
Th/U	61.82	22.63	5.36	5.43	47.64	45.45	44.36	16.36	36.73	5.36	61.82	31.75	20.12
Ga/Al	2.84	2.49	2.88	3.01	2.50	2.63	3.00	2.69	2.85	2.49	3.01	2.77	0.20
Y/Nb	0.09	0.14	2.28	1.06	0.34	0.13	1.28	1.71	0.38	0.09	2.28	0.82	0.80

Continued

Y+Nb	31.75	21.75	59.00	111.00	39.00	53.00	185.00	203.00	69.00	21.75	203	85.83	66.62
Avg MPa[1]	871	767	1075	1481	878	830	842	876	665	665	1481	920.56	236.50
Depths[2]	23.5	20.7	29.0	40	23.7	22.4	22.7	21.2	18	18	40	24.58	6.49
Aμ·Wm^{-3}	13.15	15.26	9.41	15.27	10.42	9.98	9.72	4.34	8.27	4.34	15.27	10.65	3.48

Note: [1,2]Blundy and Cashman (2001) [26].

Table 4. CIPW normative composition of Kathalguri Granite.

	APD/K1	APD/K2	APD/K3	APD/K4	APD/K5	APD/K6	APD/K7	APD/K8	APD/K9
Q	23.64	24.52	22.00	18.27	23.67	23.95	21.99	24.09	24.03
C	0.51	0.29	0	0	0	0.40	0	0.21	0
Or	36.05	33.86	35.16	34.16	37.05	35.64	31.97	34.10	33.92
Ab	28.94	30.46	30.89	19.29	27.42	27.75	20.05	30.80	32.90
An	5.15	5.45	5.36	8.66	6.09	5.53	7.79	4.39	0.00
Ac	0.00	0.00	0.00	0.00	0.00	0.00	0.00	0.00	0.68
Di	0.00	0.00	0.16	2.87	0.14	0.00	2.76	0.00	4.58
Hy	2.78	2.69	2.85	8.41	3.08	3.28	6.94	3.01	1.28
Mt	1.09	1.13	1.17	3.35	1.14	1.35	3.02	1.33	1.11
Il	0.48	0.42	0.49	2.24	0.49	0.46	2.00	0.44	0.48
Ap	0.24	0.17	0.17	1.49	0.21	0.19	1.23	0.12	0.17
Sum	98.87	98.98	98.25	98.74	99.30	98.53	97.75	98.48	99.15

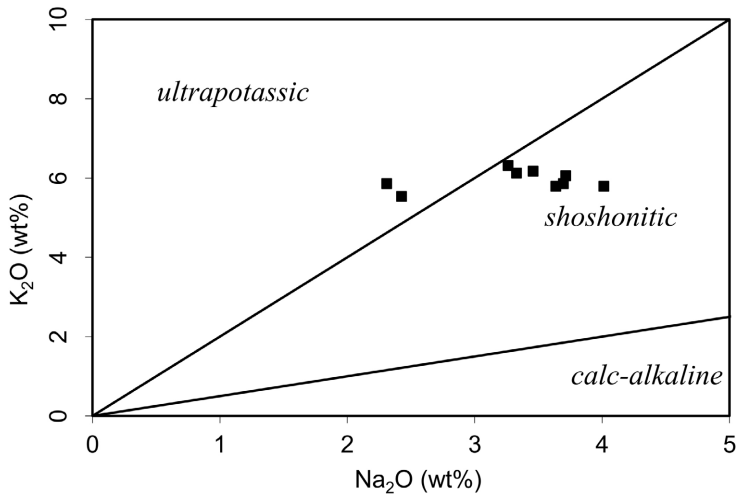

Figure 15. K_2O vs Na_2O plot after Peccerillo and Taylor 1976 [27] for Kathalguri Granites.

Sun and Macdonough 1989 [25] showing depletion in Sr, P, Ti, Y (n = 2) and enrichment in all other elements (**Figure 14(b)**) and pronounced negative Eu anomaly. Kathalguri Granites are characterized by enriched LREE and depletion of HREE. The ΣLREE varies from 246.73 to 531.04 and ΣHREE 45.10 to 162.86. Eu/Eu* varies between 0.269 to 0.709 and mantle normalized La/Yb shows values

between 8.18 to 19.17.

The multi-elemental spider plots of Kathalguri Granite are similar to A type granite and the enrichment of elements of several times higher 1.1 to 100 times of the normalizing values indicating heterogeneity on the source materials and also indicating feldspar, apatite, ilmenite/magnetite fractionation. The SI is 7.32 - 18.29, LI 14.8 - 25.82, and DI varies from 75.49 - 92.16, averaging 86.86. The K_2O-Na_2O relationship offers shoshonitic to high potassium series composition (**Figure 15**). As the extreme FeO^T enrichment relative to MgO resulting in high FeO^T/MgO 2.93 - 7.49 is a typical signature of A-type granitoids (Frost *et al.*, 2001) [28], all the samples are grouped as ferroan A-type granite in {FeO^T/(FeO^T + MgO)} vs SiO_2 diagram (**Figure 16**).

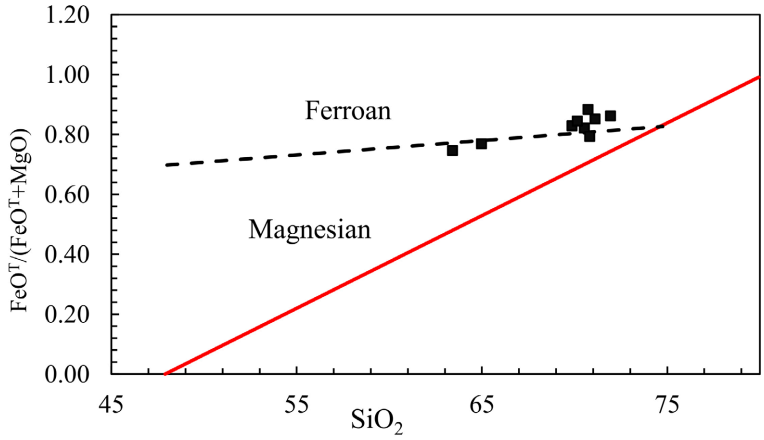

Figure 16. Chemical classification of Kathalguri Granites using FeO*/(FeO + MgO) vs SiO_2 diagram after Frost *et al.* (2001) [28].

The mol Al_2O_3/(CaO + Al_2O_3 + K_2O) (A/CNK) values range from 0.83 to 1.02, but average is <1.00 (0.95). In the A/NK vs. A/CNK diagram, most of the samples are predominantly plotted in the metaluminous field n = 4 samples fall in the peraluminous field, while one sample falls in the peralkaline field. (**Figure 17**)

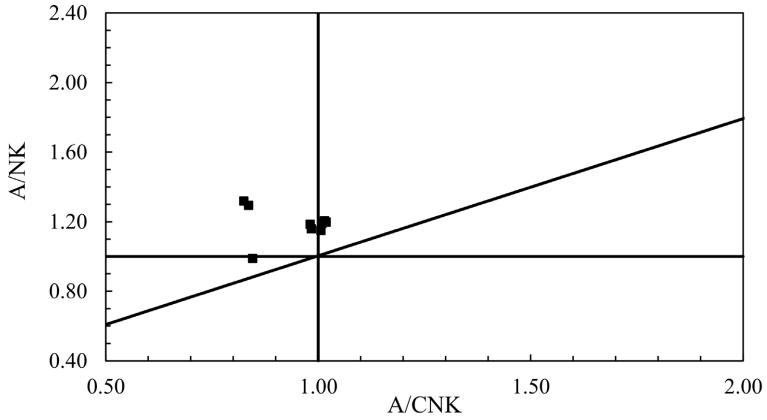

Figure 17. A/CNK vs A/NK for Kathalguri Granite showing metaluminous to peraluminous character in Shands Index diagram modified after Maniar and Piccoli (1989) [29].

It has Normative Corundum n = 4 samples (Table 4) indicating either it has intruded and assimilated some metapelites or clay rich sediments (Tyrsad argillaceous and arenaceous Barapani formations) or fractional crystallization, as magma cools and crystallizes, certain minerals preferentially form and remove specific elements from the melt. The Kathalguri Granites have elevated levels of radioelements (U, Th and K).

7. Petrogenesis

The K vs Rb plot shows the samples plot below the crustal value of K/Rb = 250. They lie between 98 and 214 with an average of 149 (Figure 18(a)) indicating its evolved nature (Taylor, 1965; Rossi *et al.*, 2011) [30] [31], while the average of magmatic rocks is given as 230, with most of the crustal rocks ranging from 150 to 350 (Taylor, 1965) [30]. K/Ba values show a departure from the crustal average of 65 (Mason 1966) [32] for Kathalguri Granite only two samples fall below 65 while others show >65 (Figure 18(b)). Ba-Rb diagram of (after Mason 1966) [32], Kathalguri Granite samples are plotted below the crustal line Ba/Rb = 4.4 (Figure 18(c)), the plots are located in between the line Ba/Rb = 4.4 to Ba/Rb = 4.4 × 10^{-1}. This indicates their derivation from crust at moderate levels (intermediate crust). The Rb-Sr binary plot shows that the Kathalguri Granites have been derived from highly differentiated and evolved granite with DI varying from 75.49 - 91.16 with an average of 86.86. It has high $FeO^{(T)}$/MgO varying from 2.93 - 7.49, averaging 4.92, specifically around SiO_2 70%. It shows the high values of $FeO^{(T)}$/MgO due to high $FeO^{(T)}$ and occupies the Ferroan field, while only two samples fall in the Magnesian field in SiO_2 vs $FeO^{(T)}/(FeO^{(T)}+MgO)$ Figure 18(d) after Frost *et al.* (2001) [28].

Multicationic R1 vs R2 binary plot according to classification of Batchlor and Bowden 1985 [33] Kathalguri Granite is anorogenic granite only two samples (APD/K/4 and APD/K/7) plot along the line between late orogenic and post collisional uplifts (Figure 19(a)), also indicating assimilation of pelites during the ascent also supported by ternary plot after Laurent 2014 [34] (Figure 19(b))

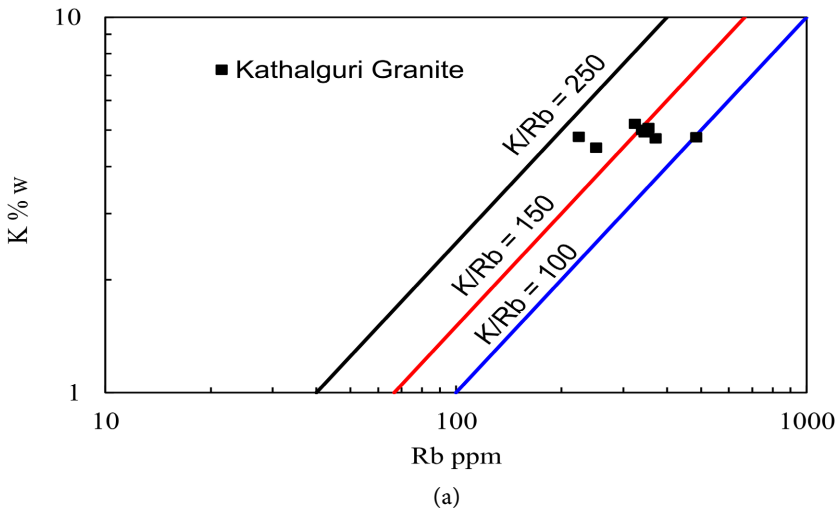

(a)

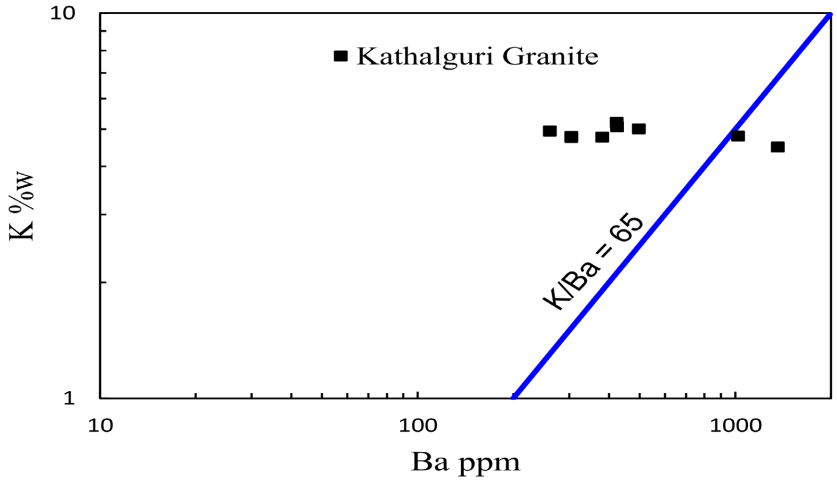

(b)

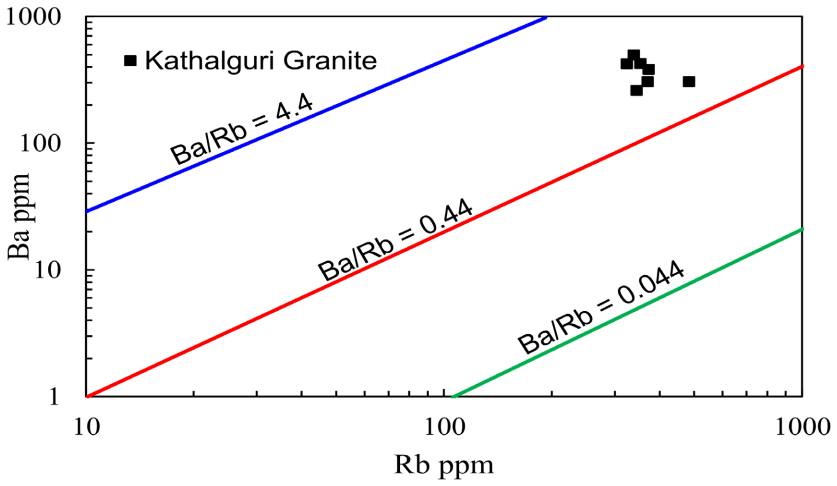

(c)

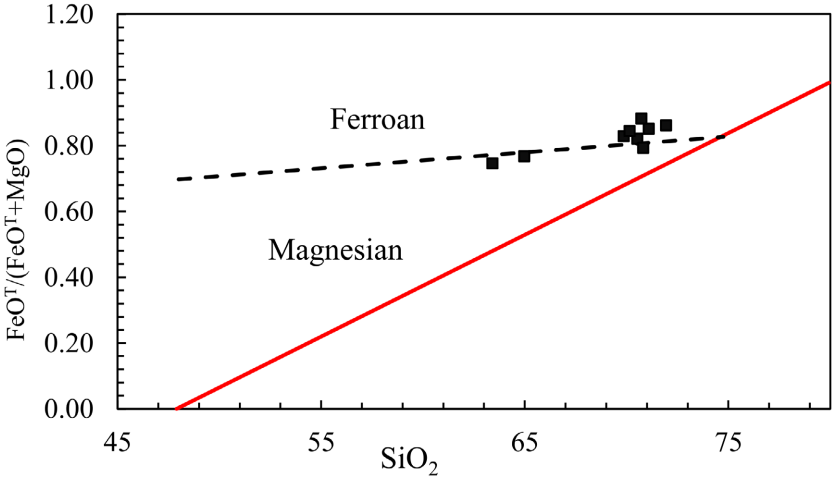

(d)

Figure 18. (a) The K vs. Rb diagram after Taylor, 1965 [30] for Kathalguri Granite. (b) The K vs Ba diagram after Mason 1966 [32] for Kathalguri Granite. (c) Rb vs Ba plot after Mason 1966 [32] for Kathalguri Granite. (d) Chemical classification of Kathalguri Granites using FeO*/(FeO + MgO) vs SiO_2 diagram after Frost *et al.* (2001) [28].

where all the samples of Kathalguri Granite plot in metasediment field. The $Na_2O + K_2O + Fe_2O_3 + MgO + TiO_2$ vs. $(Na_2O + K_2O)/(Fe_2O_3 + MgO + TiO_2)$ plot after Patiño Douce 1999 [35] (**Figure 20**) shows evidence of a melt of crustal metagraywackes magma source. The experiments indicate that the meta-graywackes contain biotite and plagioclase but no aluminosilicates.

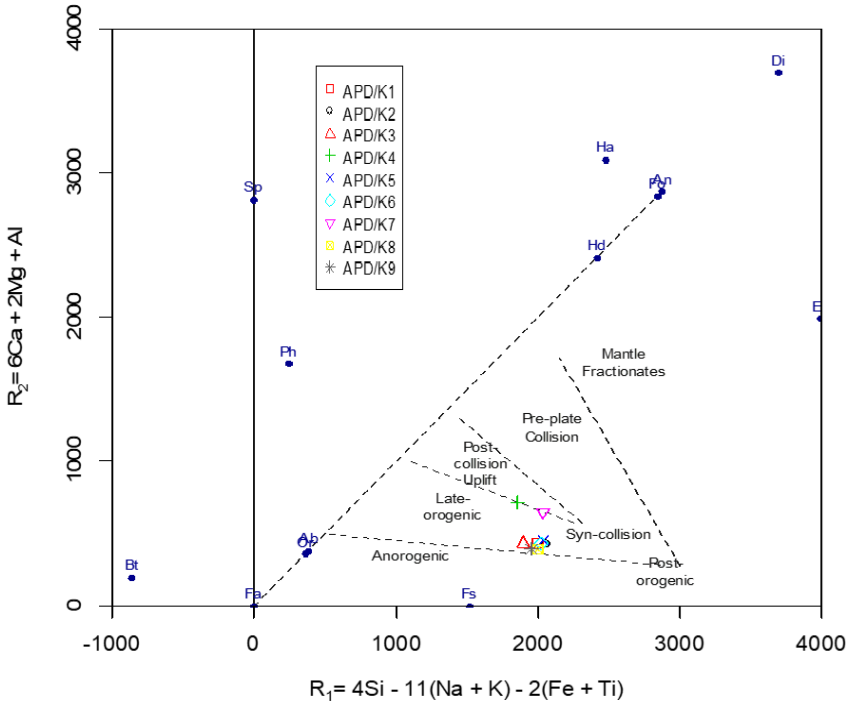

(a)

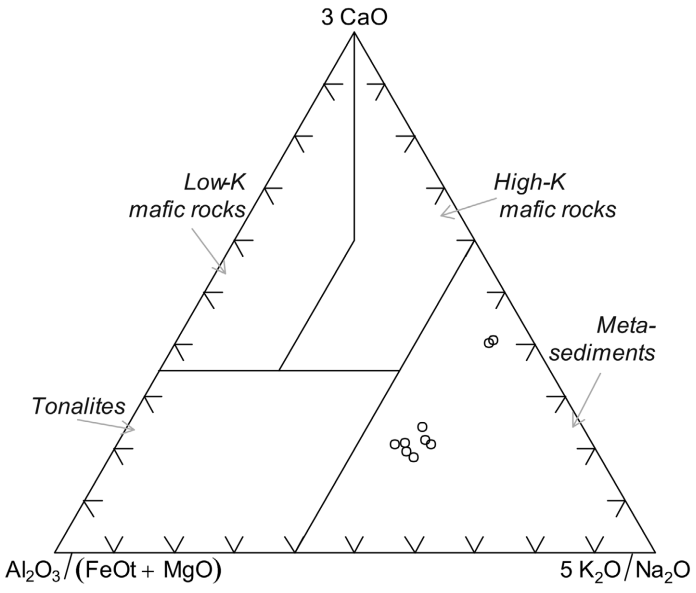

(b)

Figure 19. (a) R1-R2 plot after Batchelor and Bowden 1985 [33] for Kathalguri Granite. (b) Source diagram after Laurent *et al.* 2014 [34] for Kathalguri Granite showing is source by metasediments.

The low Mg# (3.91 to 9.88) indicates a highly evolved magmatic source. It suggests that the magma from which this granite crystallized had undergone significant fractional crystallization, removing early-formed mafic minerals rich in Mg and Fe, leaving behind a melt enriched in silica and alkalis. SiO_2 vs Mg# plots (**Figure 20**) indicate an evolved magmatic origin, with significant fractional crystallization and possible crustal contamination.

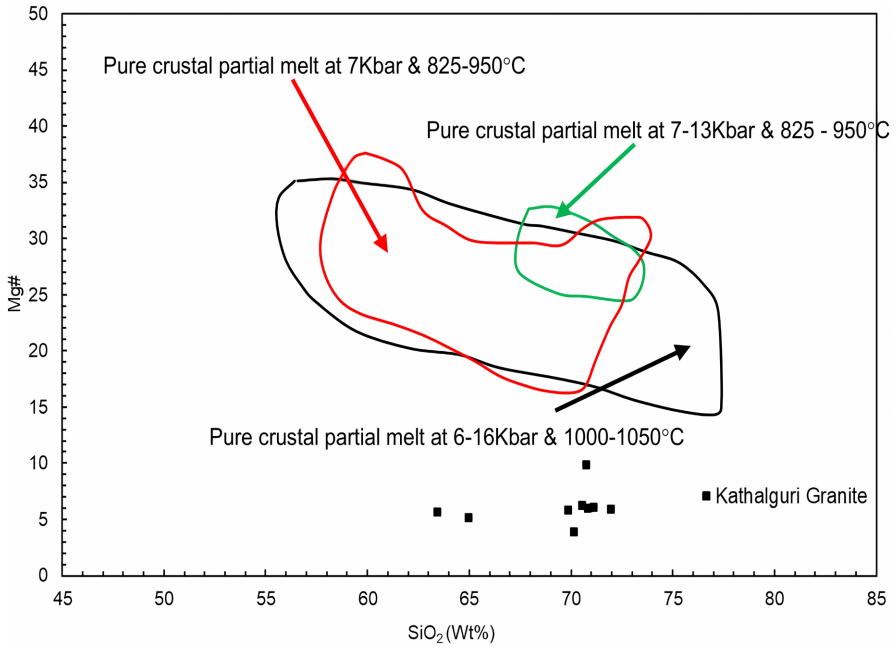

Figure 20. Mg# = 100*[Mg/(Mg + Fe^T)] vs. SiO_2 diagrams for Kathalguri Granite. The fields of pure crustal partial melts determined in experimental studies are from Jiang *et al.* (2013) [36]. The fields of pure crustal partial melts obtained in experimental studies by dehydration melting of low-K basaltic rocks at 8 - 16 kbar and 1000˚C - 1050˚C (Rapp and Watson 1995) [38], of moderately hydrous (1.7% - 2.3% H_2O) medium- to high-K basaltic rocks at 7 kbar and 825˚C - 950˚C (Sisson *et al.*, 2005) [39], and of pelitic rocks at 7 - 13 kbar and 825˚C - 950˚C (Rapp *et al.* 1991) [37].

The tectonic setting is likely extensional, such as rift zones or post-orogenic environments, where the conditions favour the production and emplacement of highly evolved, silica-rich magmas. The trace elemental contents (Zr + Nb + Ce + Y) >340 and high 10^4 × Ga/Al values ranging from 2.49 - 3.01 averaging 2.77 (>2.6), are characteristics of the A-type granite after Whalen *et al.* 1987(**Figure 21**) [40]. Ternary plot after Eby (1992) [41] Fe_2O_3*5-(Na_2O + K_2O)-[(CaO + MgO)*5] shows two sample plots in A2 and remaining all (n = 7) sample plot in A1 type granite field (**Figure 22**), thus illustrates a continuous shift from post-collision A2 to post-orogenic A1-Type. A similar pattern is shown in ternary plots of Nb, Y, Ce; Nb Y and 3Ga after Eby 1992 [41] (**Figure 22(b)** and **Figure 22(c)**). In Nb-SiO_2 diagram proposed by Pearce and Gale (1977) [42], all granitic samples plot in the within plate magma field with only one sample falling in the vicinity of crustal melts field (**Figure 23**).

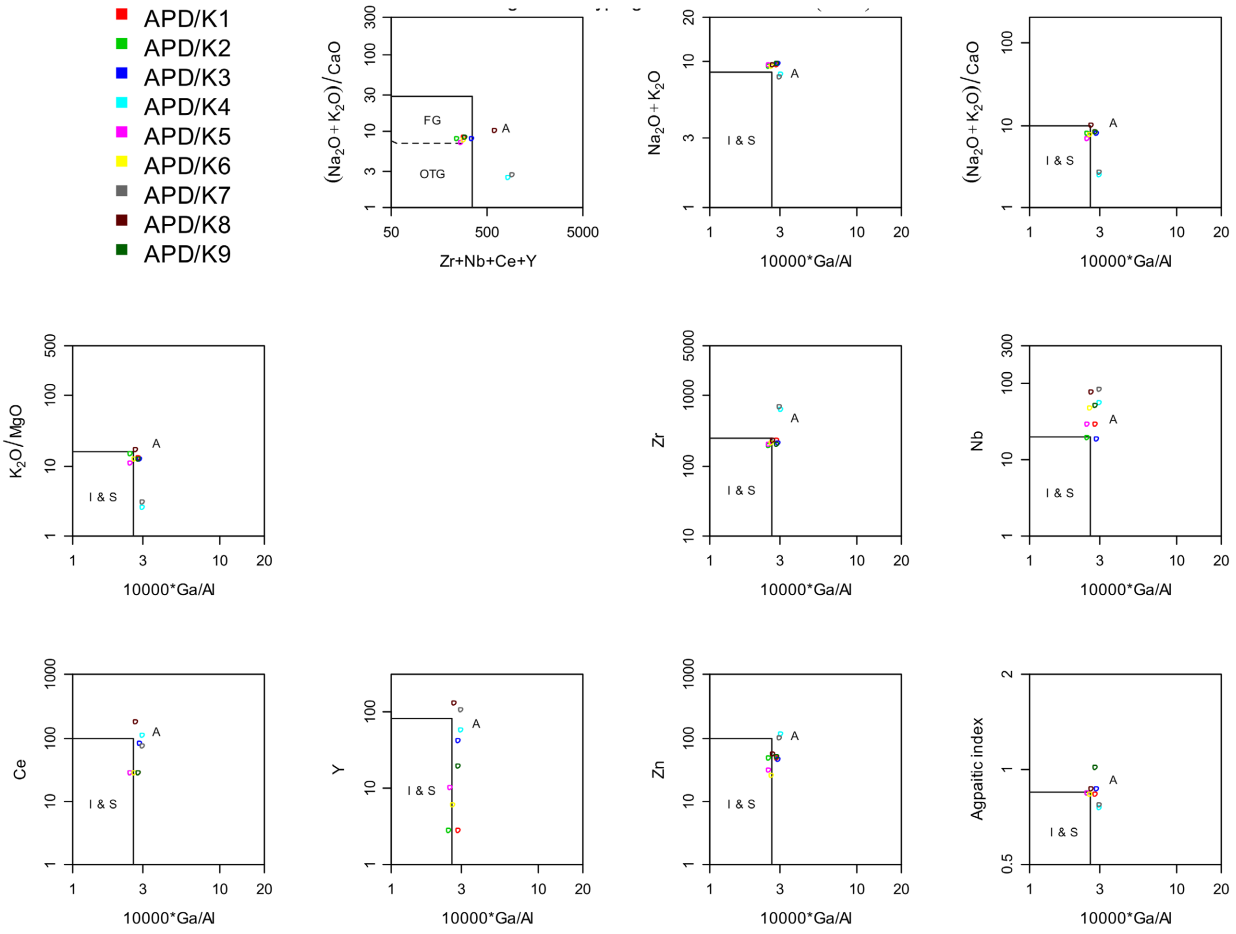

Figure 21. Discriminant diagram for Kathalguri Granite after Whalen *et al.* 1987 [40].

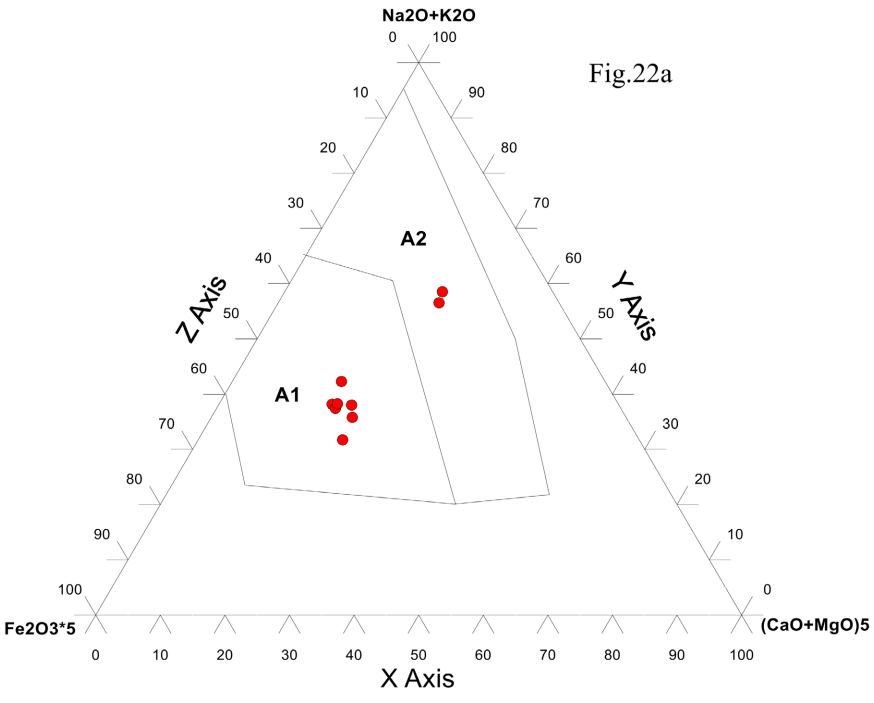

Fig.22a

(a)

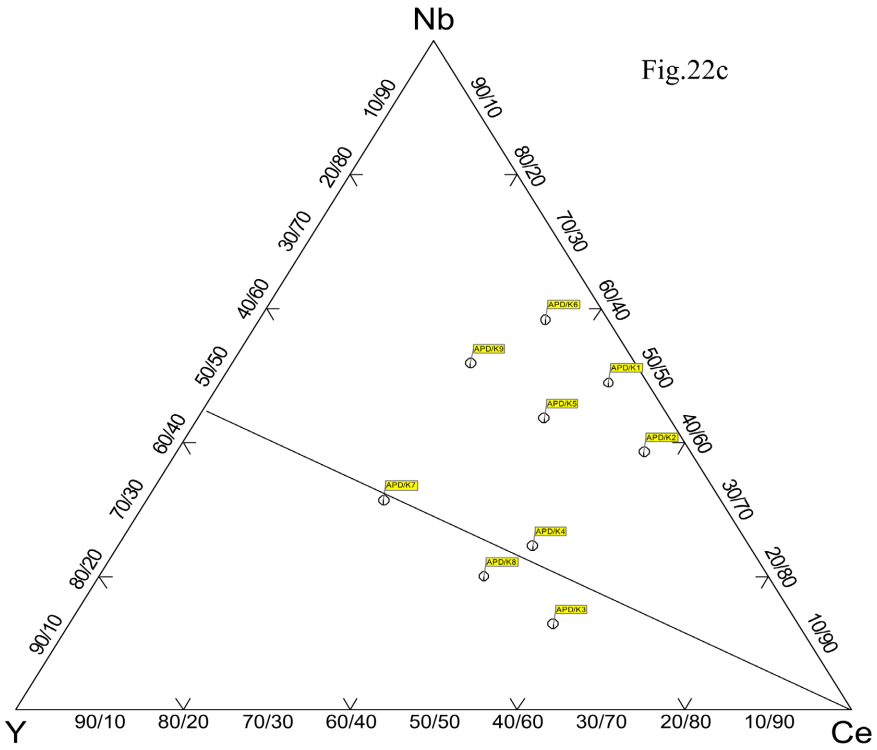

(b)

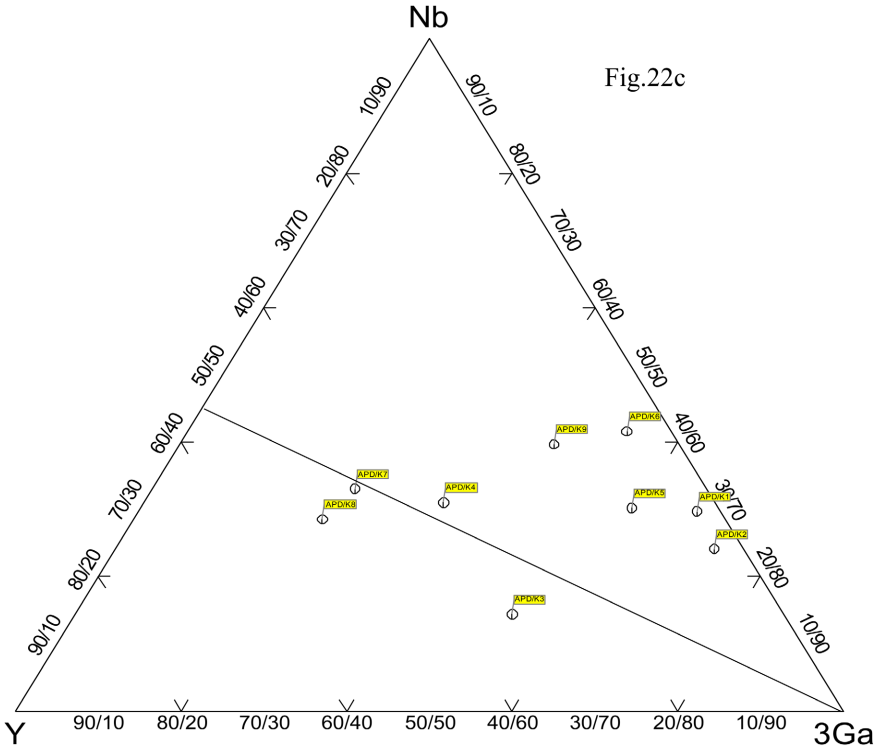

(c)

Figure 22. Ternary plots after Eby 1992 [41] for Kathalguri Granite occupying A1 type granite (n = 6 Samples while (Truly Anorogenic Rifting), and only two samples plot (APD/K/3 and APD/K/8) in A2 type (Post-Collisional) field. (a) Fe_2O_3*5-(Na_2O + K_2O)-[(CaO + MgO)*5], (b) Ce-Y-Nb and (c) 3Ga-Y-Nb plot.

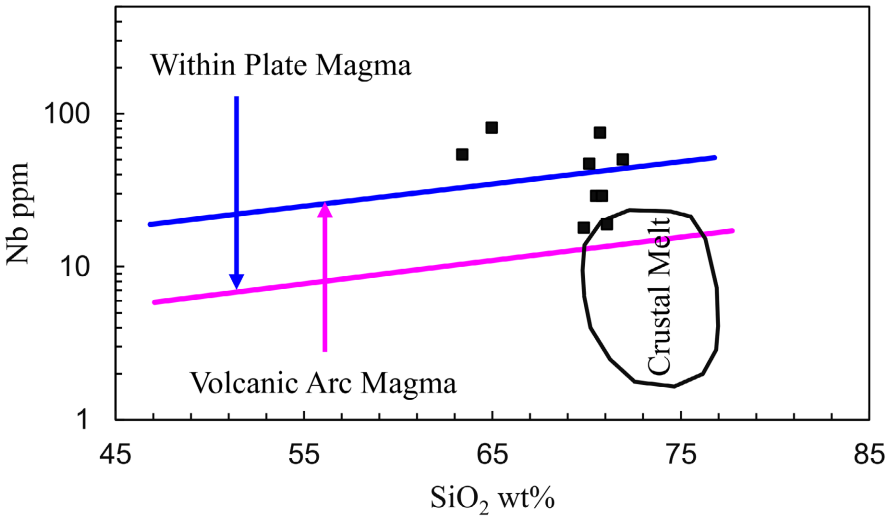

Figure 23. Nb-SiO_2 plot (after Pearce and Gale, 1977) [42].

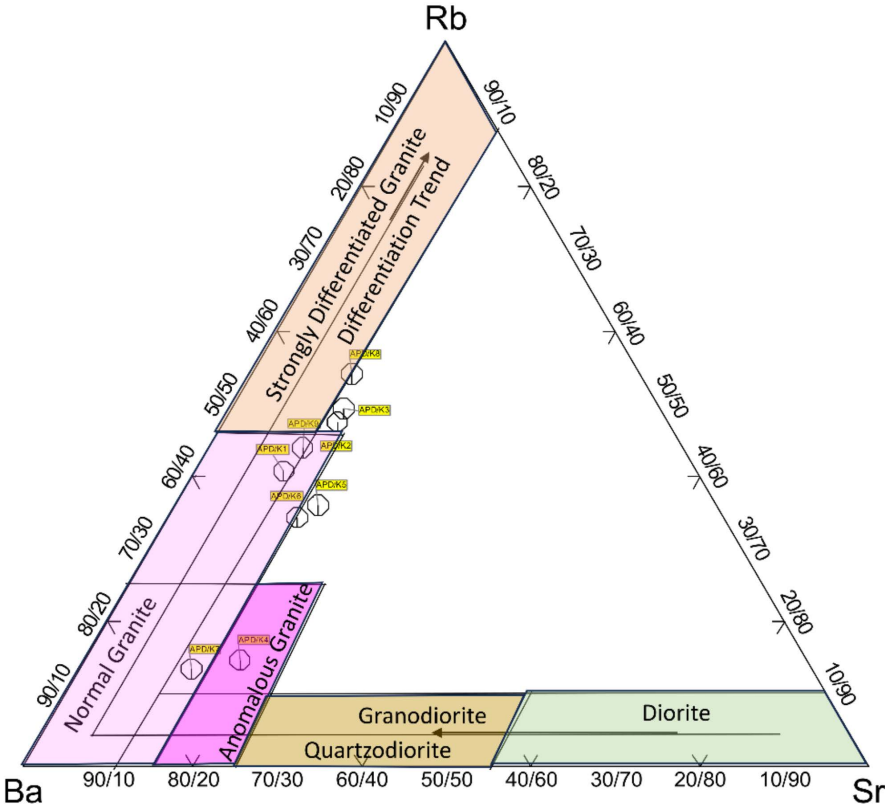

Figure 24. Rb-Ba-Sr ternary diagram after El Bouseily and El Sokkary 1975 [55] for Kathalguri Granite showing Anomalous-normal to strongly differentiated type of granite.

Two main mechanisms are often involved in the magma production of granitoid rocks. 1) Fractional crystallisation process in magma crystallisation. (Mittlefehldt, and Miller 1983; Philips *et al.*, 1981) [43] [44] and 2) injection of melts causes a partial melting of the lower crust, followed by the absorption of crustal materials throughout the ascent (Jackson *et al.*, 1984) [45]. The geochemical data

for Kathalguri Granite indicate they are highly differentiated type granite, and have been derived by fractional crystallization.

A-type granites are formed in an extensional environment (Clemens *et al*., 1986; Whalen *et al*., 1987; Maniar and Piccoli, 1989; Eby, 1990; Bonin, 2007) [29] [40] [46]-[48]. Researchers have proposed several views on the formation mechanism of A-type granite: crystallization differentiation of mantle basaltic magma (Eby, 1990; Mushkin *et al*., 2003; Litvinovsky *et al*., 2002; Anderson *et al*., 2003) [48]-[51] mantle-derived magma mixed with crust-derived magma (Yang *et al*., 2006) [52], and partial melting of crustal materials (King *et al*., 1997; Droop *et al*., 2003) [53] [54]. High Rb/Sr 0.81 - 4.61 (average of 2.9) indicates a metaluminous (n = 4) to peraluminous (n = 4) and peraluminous (n = 1) magma source also indicates its anomalous (n = 1), normal (n = 4) to strongly differentiated (n = 3) nature in Rb-Ba-Sr ternary diagram after El Bouseily and El Sokkary 1975 [55] (**Figure 24**).

The Kathalguri Granite is moderately oxidized (**Figure 25**) and belongs to magnetite series of Ishihara (1977) [56].

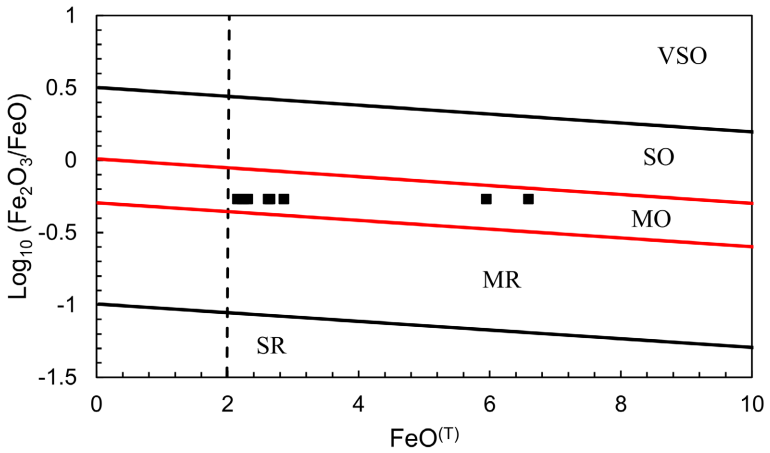

Figure 25. Plot of $\log_{10}Fe_2O_3/FeO$ vs. $FeO^{(T)}$ for redox classification (after Blevin, 2004) [57] VSO = very strongly oxidized; SO = strongly oxidized; MO = moderately oxidized; MR = moderately reduced; SR = strongly reduced.

The Rayleigh fractionation model and the distribution coefficient for particular elements between distinct melt and mineral phases were used to quantitatively estimate the fractional crystallization trend of minerals (Sylvester, 1998; Wu *et al*., 2017) [58] [59]. The Large Ion Lithofile (LIL) modeling is used to decipher the plagioclase, Biotite and K-feldspar and plagioclase fractionation trends are shown in bivariate Log-Log plots of Rb-Sr and Rb-Ba (**Figure 26(a)**, **Figure 26(b)**), Similar fractionation of K-feldspar, plagioclase and biotite is shown by Eu vs Rb and Eu vs Ba bivariate plots. The fractionation trend from mantle derived rocks is also revealed by Cr vs Ni plot (**Figure 26(c)**). Low Al_2O_3/TiO_2 at high CaO/Na_2O (**Figure 26(d)**) is consistent with the involvement of possible mafic source materials, and implies that for the Kathalguri Granite. Each plot shows a vector of net change in the composition of the fluids after 30% Rayleigh Fractionation. Ba vs Eu plot also depicts biotite and K-feldspar fractionation vectors (**Figure 27(a)**).

La vs $(La/Yb)^N$ bivariate plot shows Zr and REE fractionation vectors (Figure 27(b)). Rb/Nd vs Rb plot (Figure 27(c)) shows partial melting and Rb/V vs Rb Log-Log plot (Figure 27(d)) shows both mixing and fractional crystallization

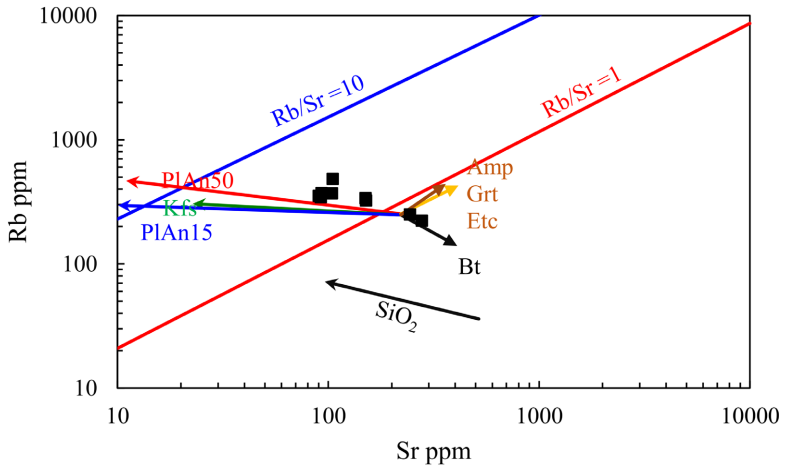

(a)

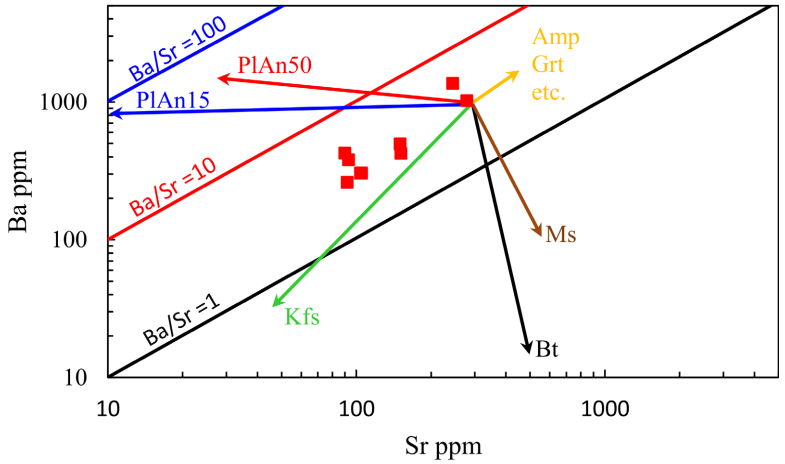

(b)

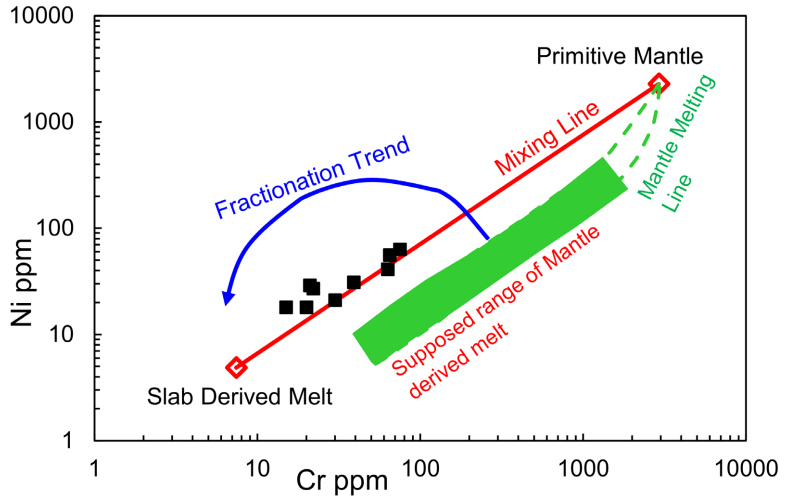

(c)

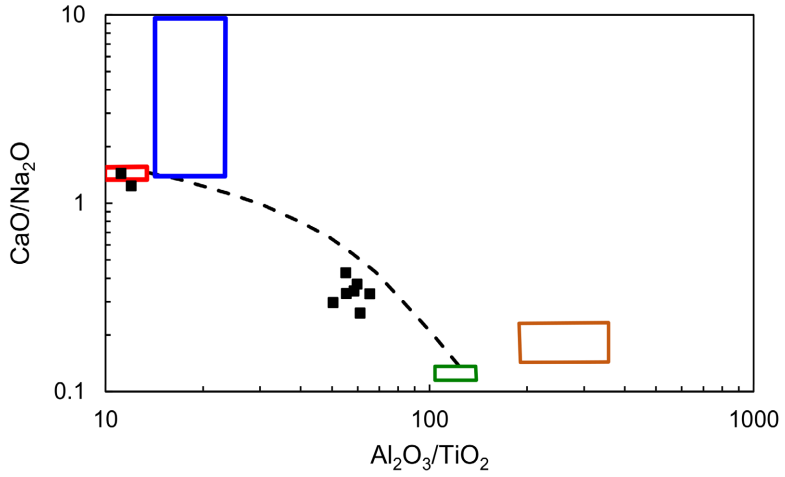

(d)

Figure 26. Chemical discrimination diagrams illustrating the mineral fractionation process for the Kathalguri Granite. (a) Rb versus Sr, (b) Ba versus Sr Abbreviations: Bt, Biotite; Ms, Muscovite; Cpx, clinopyroxene; Hbl, hornblende; Kfs, K-feldspars; Plg, plagioclase; Amph, Amphibole, Grt, Garnet. Plots after Sylvester 1998, Wu *et al.* 2017 [58] [59]. (c) Cr vs Ni Plot for Kathalguri Granite showing fractionation trend. (d) Kathalguri Granite in CaO/Na_2O vs Al_2O_3/TiO_2 plot. The "MORB" (red rectangle) composition is compiled from GERM database http://earthref.org/, and "Pelite-derived melt" (green rectangle) field is from Patiño Douce and Johnston (1991) [61]. The compositions of the eclogitic amphibolites (blue rectangle) likely part of the lower plate involved in the Variscan collision (Medaris *et al.* 2003) [62], and the average composition of country-rock metasediments (orange rectangle). Kathalguri Granite showing enriched mantle-derived and crustally-derived melts by occupying compositional field in between MORB to Pelite-derived melt position.

trends after Schiano *et al.* (2010) [60]. The negative correlations of SiO_2 and $FeO^{(T)}$ also indicates Fe-Ti oxides fractionation (**Figure 27(e)**). The most likely mechanism is crystal fractionation suggested by modeling and subordinate partial melting and mixing models. Similarly, negative correlation SiO_2 and Zr (**Figure 28(b)**) also indicates Zircon fractionation or zircon overgrowth as seen on several zircon crystals (**Figure 12(d)**).

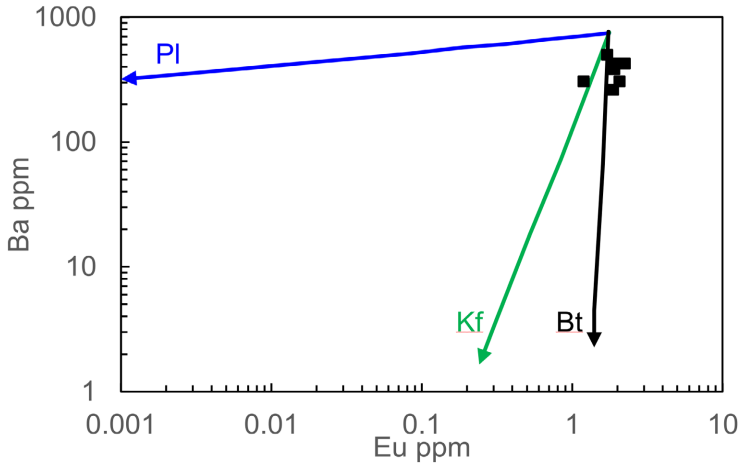

(a)

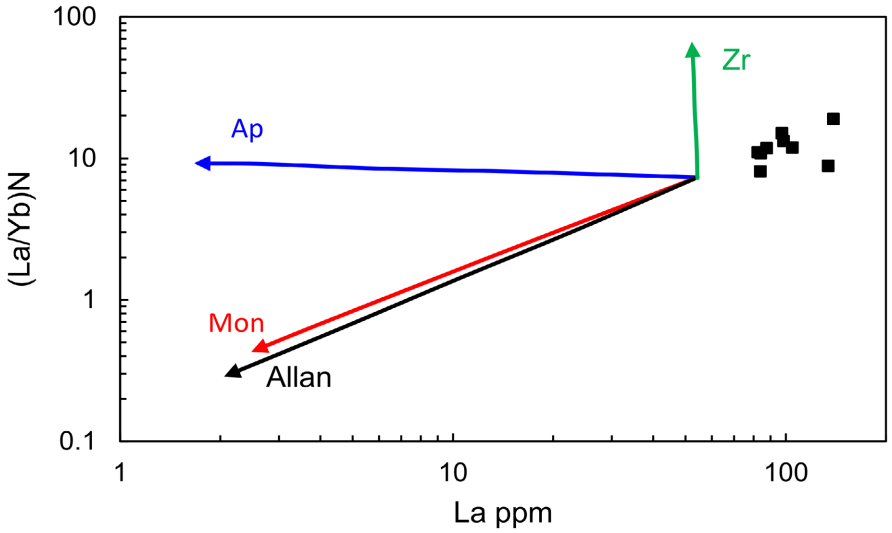
100
10
1
0.1
(La/Yb)N
Zr
Ap
Mon
Allan
1
10
100
La ppm

(b)

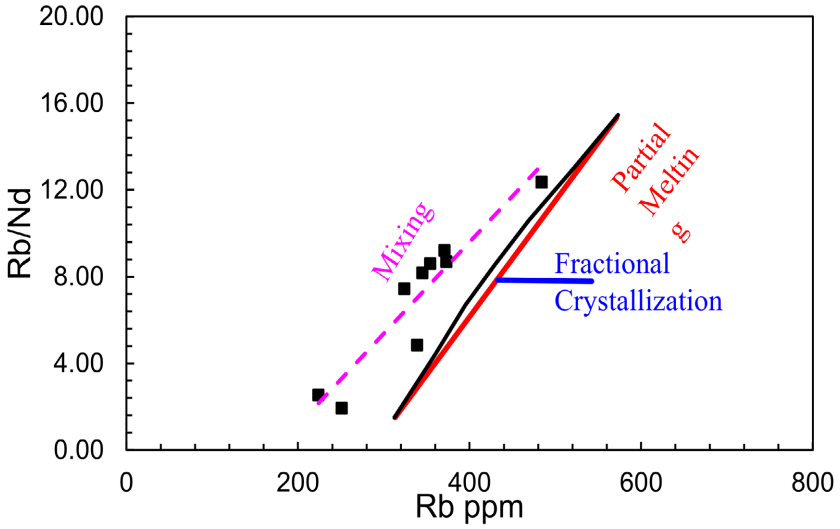
20.00
16.00
12.00
8.00
4.00
0.00
Rb/Nd
Mixing
Partial Melting
Fractional Crystallization
0
200
400
600
800
Rb ppm

(c)

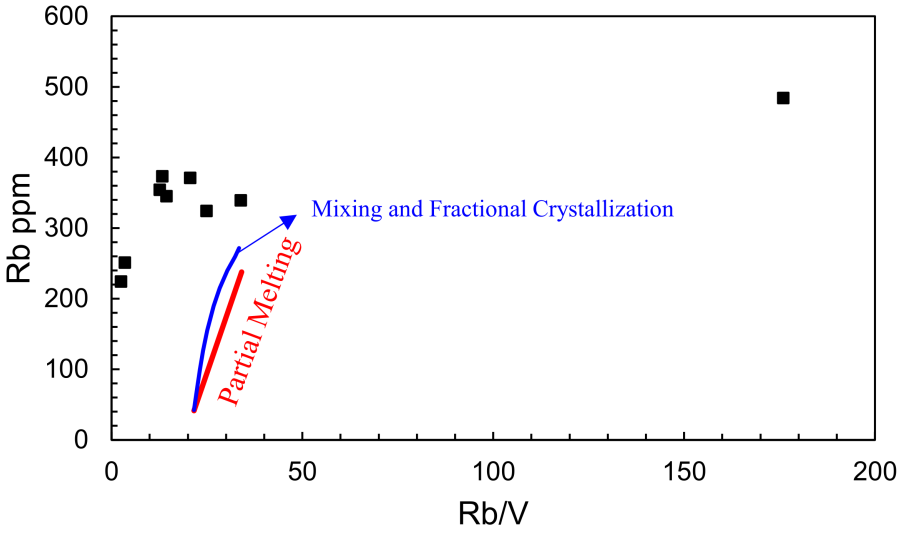
600
500
400
300
200
100
0
Rb ppm
Mixing and Fractional Crystallization
Partial Melting
0
50
100
150
200
Rb/V

(d)

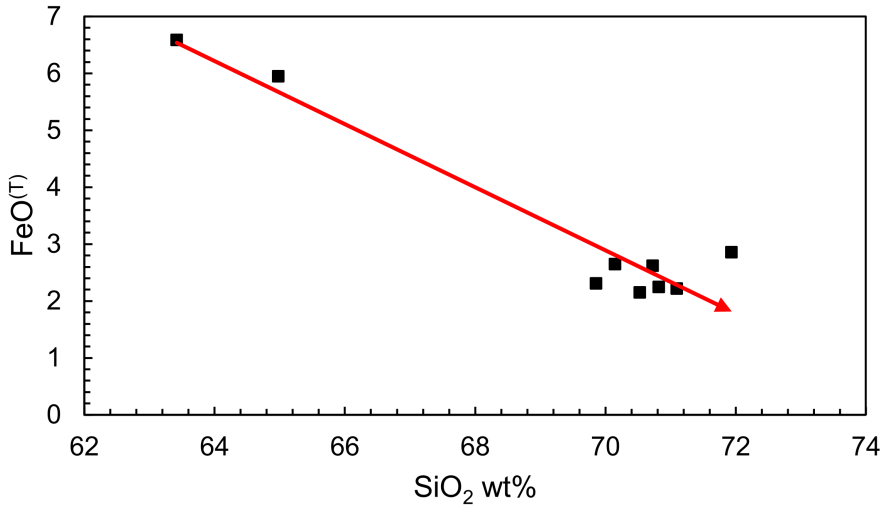

(e)

Figure 27. (a) Ba vs Eu plot. (b) La vs (La/Yb)N plot. (c) Rb vs Rb/Nd plot. (d) Rb/V vs Rb plot showing Mixing and Fractional crystallization trends after Schiano *et al.* (2010) [60]. (e) SiO_2 vs $FeO^{(T)}$ plot showing negative correlation indicates fractionation of feldspar and Fe-Ti oxides.

8. Geothermobarometry

All the analysed samples Kathalguri Granite have whole-rock chemical compositions that fall in the range of M < 2 (M = {(Na + K + 2Ca)/(Al*Si)} as constrained by Watson and Harrison (1983) [63] there also the temperature ranges between 779˚C - 882˚C with an average of 815˚C, and for comparison also by Boehnke *et al.* (2013) [64] model, since it has wt% SiO_2 within the range of 63.42% - 71.94%. The Kathalguri Granites yield maximum zircon saturation temperatures (*T*zr) between 721˚C - 834˚C with an average of 766˚C (**Table 5**, **Figure 28(a)**). Rutile saturation thermometry by Ryerson and Watson (1987), Hayden and Watson (2007) [65] [66] were also used and the temperature range 783˚C - 927˚C with an average of 820˚C is found to be higher (**Table 5**) than the Zircon saturation temperatures by Watson and Harrison (1983) [63]. The magma redox condition can be qualitatively assessed using whole-rock ferric to ferrous Fe ratios of granites (Blevin, 2004) [57]. Kathalguri Granites exhibit the highest Fe_2O_3/FeO ratios of 0.538 and plots in the fields with moderate oxidation (**Figure 25**). Zircon also shows negative correlations with SiO_2 (**Figure 28(b)**). The average pressure of co-crystallization of quartz, albite and orthoclase and depth of intrusion are constrained after Yang 2017 [67] revealed that they were crystallised at a depth range of 14 - 27 km at a pressure range of 5 - 10 kbars, and for comparison pressure and depth of crystallisation was also made using geobarometer by Blundy and Cashman 2001 [26] (**Figure 28(c)**) results in crystallization at a pressure range of 7 - 15 kbars and depths 18 to 40 km. The cooling-crystallization period of the granitic melt is influenced by the significant concentration of Th, U and K in the melt. The high thorium content and the sympathetic relation of Th with K suggest that the

Kathalguri Granites are highly fractionated and fertile in nature. The Kathalguri Granite has elevated contents heat producing elements (U, Th and K) resulting in moderate to high heat production ranging between 4.34 to 15.27 Aμ·Wm^{-3} with an average of 10.65 Aμ·Wm^{-3} (**Figure 28(d)**). Hence, the cooling crystallization period of the Kathalguri Granite may also be controlled by the radiogenic heat production which conforms with the HHP nature of Kathalguri Granite. The high-temperature nature of Kathalguri Granite also suggests that they have been generated either in the lower crustal or upper mantle region.

Table 5. Zircon saturation temperature of Kathalguri Granite.

S. No.	M	Zr.obs	Zr.sat	[1]TZr.sat.˚C	[2]TZr.sat.˚C	[3]TRt.sat.˚C. HW
APD/K1	1.48	231	194.8	812.6	768	794.4
APD/K2	1.48	192	195.9	795.6	747.9	783
APD/K3	1.54	206	208.9	797.7	748.6	796.4
APD/K4	2.00	618	355.4	864.7	810.7	927.4
APD/K5	1.53	201	207.7	795.9	746.6	795.7
APD/K6	1.48	207	196.1	802.3	755.6	790.4
APD/K7	1.90	676	318.4	882	834.4	920.7
APD/K8	1.48	224	196.4	809.3	763.8	787.4
APD/K9	1.75	199	266.7	779	720.5	787.2
Average				815.5	766.2	820.3

NB: [1]Watson & Harrison (1983) [63], [2]Boehnke (2013) [64], [3]Ryerson and Watson (1987) [65].

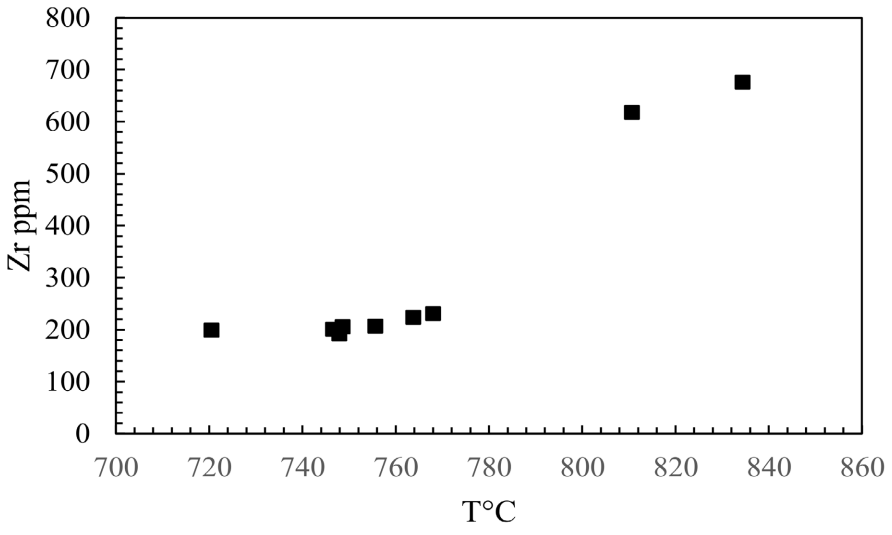

(a)

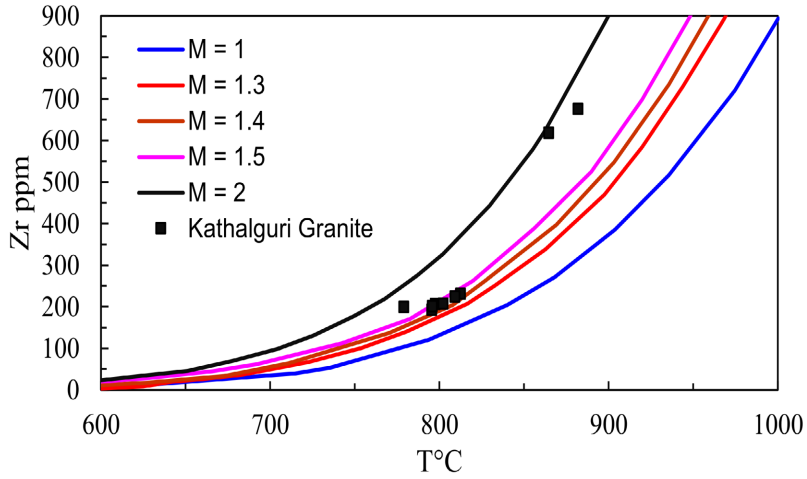

(b)

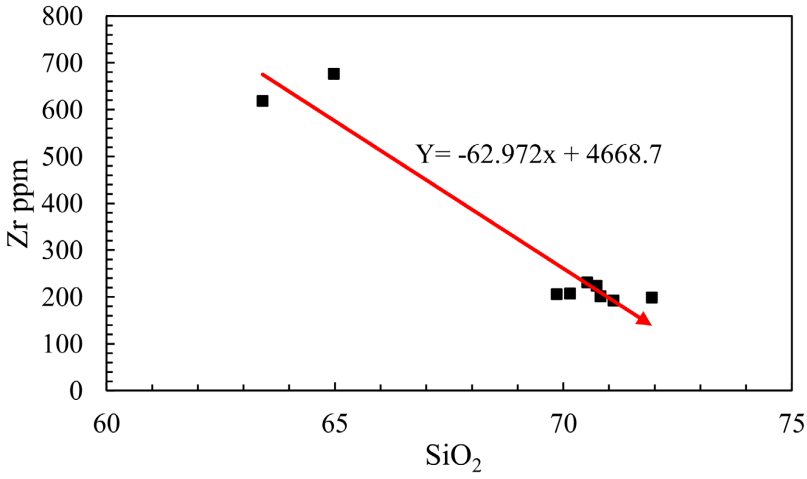

(c)

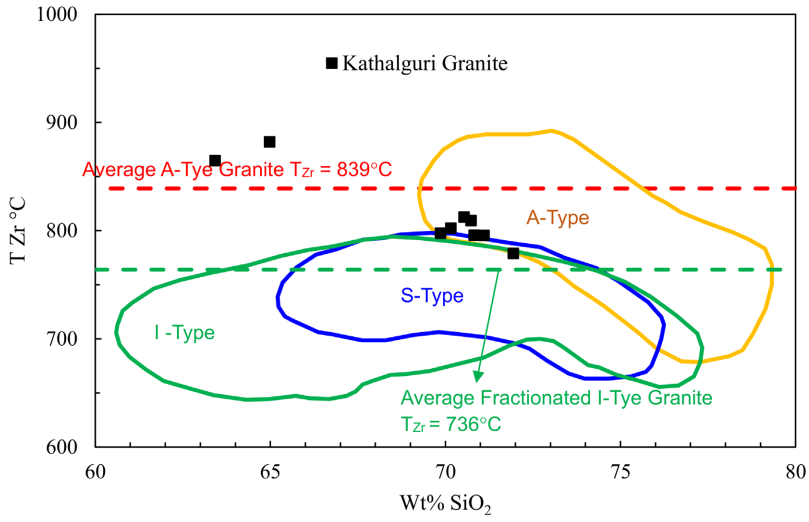

(d)

Figure 28. (a) Zircon Saturation Temperature vs Zr plot. (b) TZr vs Zr plots with M fences. (c) SiO_2 vs Zr plot showing negative correlation. (d) SiO_2 vs T_{Zr} plot for Kathalguri Granite showing it's a type characteristic.

9. Geochronology

Nine samples from Kathalguri Granites were collected (Figure 3, Figure 4) and analysed for Rb-Sr, Sm-Nd, and Pb-Pb isotopic systematics. The isotopic analysis reveals that the Kathalguri Granite contains 274 - 414 ppm Rb and 95 - 277 ppm Sr. The $^{87}Rb/^{86}Sr$ and $^{87}Sr/^{86}Sr$ ratios range from 2.872 - 12.76 and 0.74004 - 0.80744, respectively (Table 7). The regression of all nine samples defines an errorchron age of 507 ± 48 Ma with an initial $^{87}Sr/^{86}Sr$ ratio of 0.7183 ± 0.0043 and MSWD of 32. However, deleting two samples, APD/K/3 and APD/K/6, which fall slightly away from the best-fit line, the seven-sample point array defines a better isochron age of 489 ± 19 Ma with an initial $^{87}Sr/^{86}Sr$ 0.7199 ± 0.0017 and MSWD of 4.1 (Figure 29(a)). $\varepsilon Sr_{(i)}$ varied between 161.62 - 332.08. This indicates that the Kathalguri Granite originated from the partial melting of ancient, evolved continental crustal material, which has undergone significant radiogenic decay over time. The Dongaon granite contains 284 - 485 ppm Rb ppm and 87.6 - 285ppm Sr 87.6 to 285 ppm. The $^{87}Rb/^{86}Sr$ and $^{87}Sr/^{86}Sr$ ratios range from 2.885 - 13.69 and 0.7394 - 0.81807 respectively (Table 8). The regression of all six samples defines an isochron age of 543 ± 41 Ma with initial $^{87}Sr/^{86}Sr$ ratio of 0.7167 ± 0.0031 with MSWD of 10.7. However, deleting one sample MHKU-3, a five-point isochron age of 558 ± 43 Ma with an initial $^{87}Sr/^{86}Sr$ ratio of 0.7159 ± 0.0029 and MSWD of 5.7 (Figure 29(b)). $\varepsilon Sr_{(i)}$ varies from 487.94 to 1603.83 suggesting complex crustal processes, such as crustal melting, recycling, or contamination, that have influenced the formation of the granite.

The results of the Sm-Nd systematics indicate that the Kathalguri Granite contains 6.50 - 21.7 ppm Sm and 39.2 - 130 ppm Nd. The $^{147}Sm/^{144}Nd$ varies from 0.0976 - 0.1029, and $^{143}Nd/^{144}Nd$ varies from 0.511556 - 0.511797. Kathalguri Granites display negative εNd(t) values −10.39 to −15.18 and eight samples regressed together do not define an isochron, and the data show considerable scatter. However, depleted mantle model ages calculated for these samples range from 1733 – 2063 Ma (Figure 30(a)). The Dengaon granite Sm and Nd contents vary from 6.58 to 20.9 ppm and 34.2 and 138 ppm. $^{147}Sm/^{144}Nd$ and $^{143}Nd/^{144}Nd$ ratios vary from 0.0903 to 0.1355 and 0.511524 to 0.511857 respectively (Table 7).

All six samples regressed together don't define an isochron, and the data show considerable scattering. However, depleted mantle model ages calculated for Dengaon granite range from 1660 to 2439 Ma. The Dengaon granite shows high negative εNd(t) ranging from −9.75 to −14.28, also hinting at some heterogeneity or multiple source contributions in the melting process. Like initial $^{87}Sr/^{86}Sr_{(I)}$ vs εNd plot (Figure 30(b)) showing continental crust and recycled crustal origin of the melts for both Kathalguri and Dengaon granites (Defant *et al.*, 1992) [68]. While plots of $(^{87}Sr/^{86}Sr)t$ versus εNdt based on Zartman & Doe, 1981 [69] (Figure 30(c)) show that the melts for the Kathalguri Granite might have been generated by Greater Himalayan metasedimentary rocks and EMII (n = 5). The results of the Pb-Pb isotopic analysis are given in Table 7. $^{206}Pb/^{204}Pb$ range from 18.371 -

20.343 and $^{207}Pb/^{204}Pb$ ratio varies from 15.697 - 15.831 except two samples APD/K/8 and APD/K/9 which have comparatively higher ratios. The regression of these samples doesn't define any meaningful isochron age due to the low spread and scatter of data points. The Dengaon granite Pb isotopic studies reveal that $^{206}Pb/^{204}Pb$ and $^{207}Pb/^{204}Pb$ ratios in these samples vary within a narrow range from 19.152 to 20.343 and 15.647 to 15.808 respectively (Table 8). The regression of these samples doesn't define any isochron age due to the scatter of data points. The high $^{206}Pb/^{204}Pb$ ratios indicate:

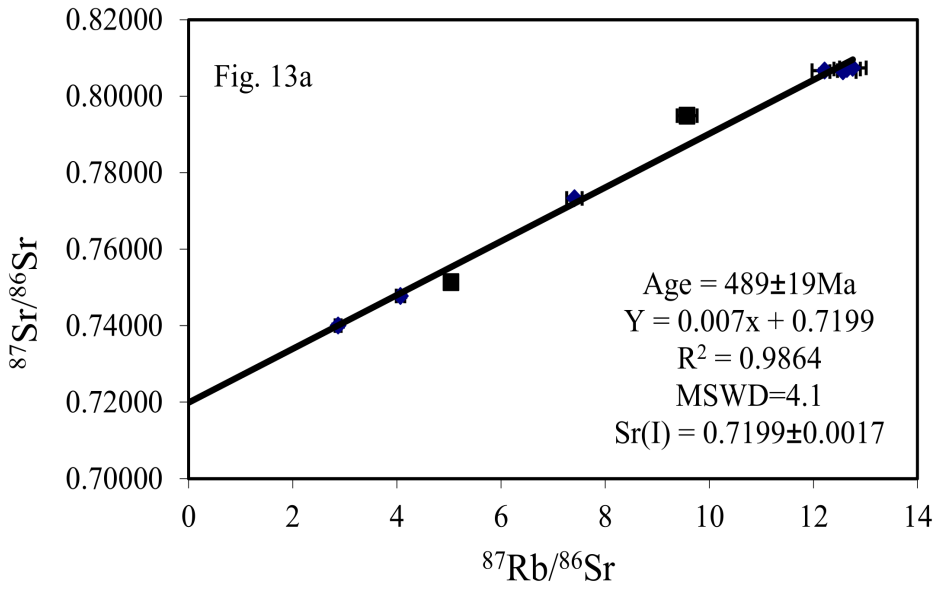

(a)

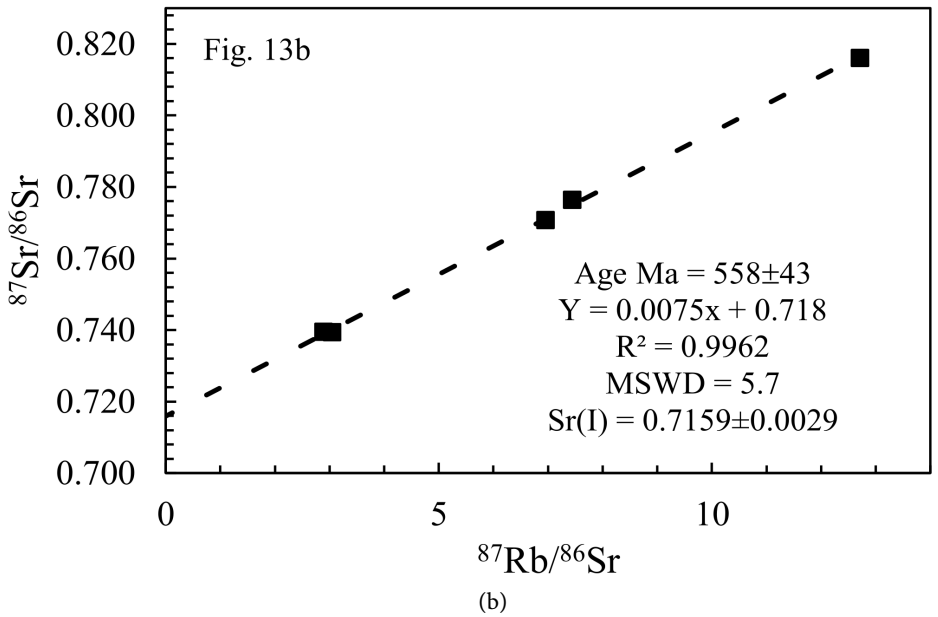

(b)

Figure 29. $^{87}Rb/^{86}Sr$ vs $^{87}Sr/^{86}Sr$ plots for Kathalguri Granite. (a) Isochron age of 489 ± 19 Ma with an initial $^{87}Sr/^{86}Sr$ 0.7199 ± 0.0017 and MSWD of 4.1. (b) Dengaon granite Isochron age of 558 ± 43 Ma with an initial $^{87}Sr/^{86}Sr$ 0.7159 ± 0.0029 and MSWD of 5.7.

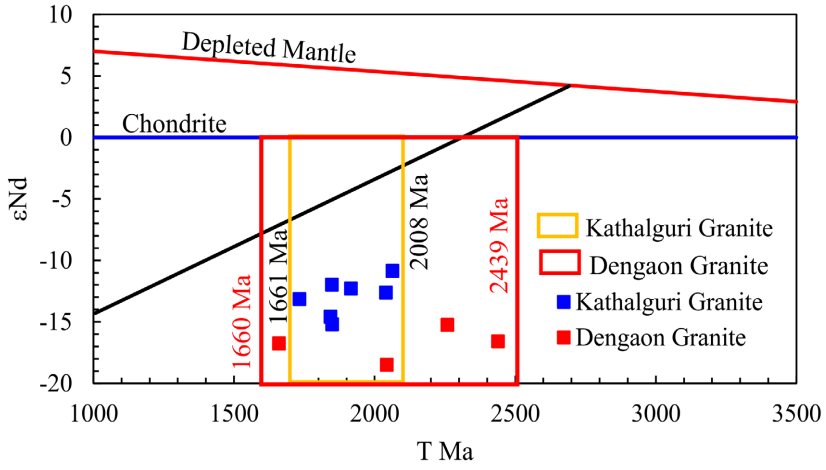

(a)

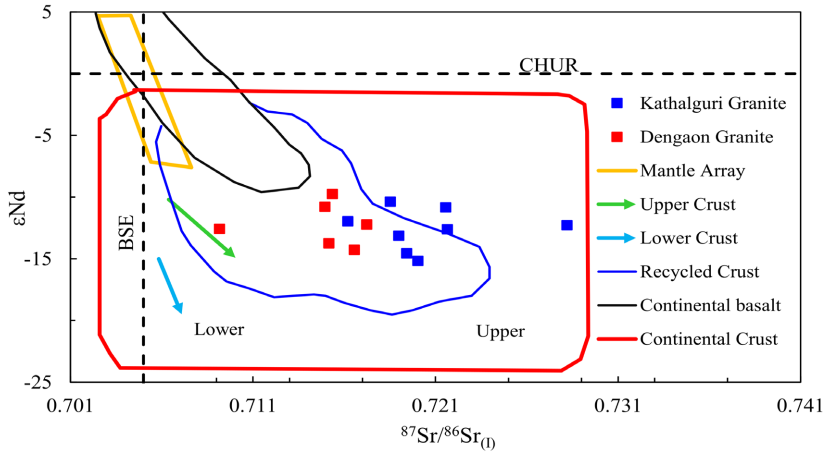

(b)

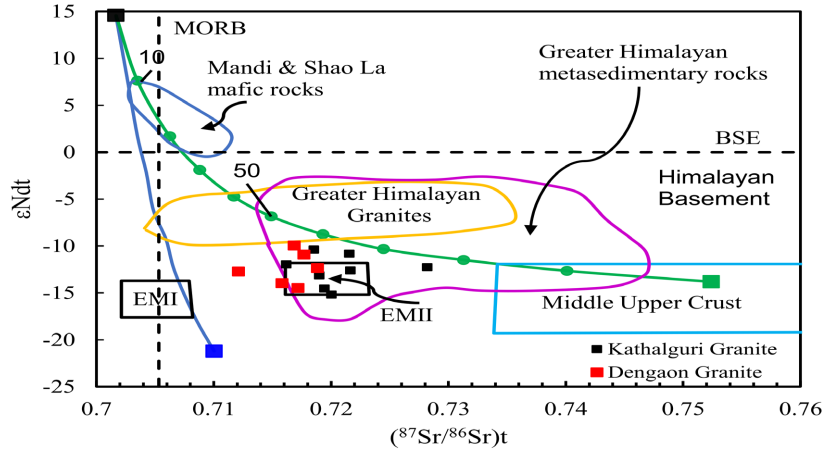

(c)

Figure 30. (a) T_{DM} vs εNd for Kathalguri and Dengaon Granite. (b) Initial $^{87}Sr/^{86}Sr_{(I)}$ versus εNd for the Kathalguri and Dengaon granite. Compared to Continental crust, recycled crust and various trends as shown in the figure. Continental crust-derived rocks field are from Defant *et al.* (1992) [68]. (c) Plots of $(^{87}Sr/^{86}Sr)t$ versus εNdt based on Zartman & Doe, 1981 [69] for Kathalguri and Dengaon granites both occupy Enriched Mantle (EMII) and greater Himalayan metasedimentary rocks field.

1. Source material with high U/Pb ratio: significant enrichment of radiogenic ^{206}Pb relative to non-radiogenic ^{204}Pb. This can happen if the source material for the rock or mineral has a high Uranium (U) to Lead (Pb) ratio. U decays to ^{206}Pb through radioactive decay, so high U content leads to more radiogenic Pb generation. The Kathalguri Granite contains elevated amounts of U 2.75 - 23 with an avg. 6.83 ppm, Th 45 - 181 ppm avg. 119.44 ppm, and Pb 2.75 - 26 ppm with an avg. of 8.93 ppm (Table 3).
2. Ancient and reworked materials: Older rocks have had more time for U decay to generate ^{206}Pb, leading to higher ratios. When such ancient materials are incorporated into younger rocks through processes like remelting or erosion, they can inherit their high $^{206}Pb/^{204}Pb$ signature. Xenoliths of older mafic rocks and Barapani arenites are seen within the Kathalguri Granite and are also supported by geochemical signatures of recycled crustal materials. Similar mafic and sedimentary patterns are also reflected by Dengaon granites.
3. Mineral-specific enrichment: presence of minerals zircon, monazite, and allanite can preferentially accumulate U/Pb, leading to high ratios within those minerals even if the bulk rock doesn't show similar values. U/Pb ratio varies 0.28 - 2.91 (avg. 1.17) and Th/Pb varies between 1 - 65.82 with an average of 30.96 (Table 3).

Similar geochemical signature like negative εNd, fractionation of feldspar, high Tzr values Guilong granodiorites have 825˚C to 875˚C but Kathalguri Granites have formed at 779˚C - 882˚C, but marked differences in Mg#. The high Mg# 43 - 46 for Guilong Granodiorite whereas the Kathalguri Granite has 3.91 - 9.88 is also observed in the granodiorites in Guilong, Southeastern Yunnan Province, Southern China (Table 6) but it has been dated much younger as 252.5 ± 1.0 Ma by U-Pb zircon dating by Liu *et al.* 2012 [70].

Table 6. Comparison of geochemical signatures of Guilong granodiorite and Kathalguri Granite.

	Guilong Granodiorite Yunan Province, China	Kathalguri Granite India, Assam India
$(^{87}Sr/^{86}Sr)i$	0.7231 - 0.7237	0.716191 - 0.721561
εNd	−29.1 to −30.4	−10.39 to −15.18 Kathalguri Granite −9.75 to −14.28 Dengaon Granite
Eu/Eu*	0.42 to 0.57	0.269 to 0.709
Mg#	43 - 46	3.91 to 9.88
(La/Yb)N	7.29 to 11.62	8.18 to 19.17
TZr	825˚C to 875˚C	779˚C to 882˚C

Table 7. Rb-Sr, Sm-Nd, and Pb-Pb data on Kathalguri Granite.

Sample ID	Rb ppm	Sr ppm	Sm ppm	Nd ppm	$^{87}Rb/^{86}Sr$	$^{87}Sr/^{86}Sr$	$^{87}Sr/^{86}Sr$ (I)	εSr	$^{147}Sm/^{144}Nd$	$^{143}Nd/^{144}Nd$	$^{143}Nd/^{144}Nd$(I)	εNd	Modal Age Ma (T_{DM})	$^{206}Pb/^{204}Pb$	$^{207}Pb/^{204}Pb$	$^{208}Pb/^{204}Pb$
APD/K/1	414	94.8	6.78	41.2	12.76	0.80744	0.718529	194.7928	0.1002	0.511797	0.511476	−10.39	1661	21.376	15.803	41.707
APD/K/2	409	94.6	6.65	40.3	12.65	0.80713	0.718985	201.2628	0.1006	0.511658	0.511336	−13.13	1853	21.268	15.831	41.811
APD/K/3	385	117	6.87	42.2	9.576	0.79493	0.728205	332.0800	0.0991	0.511679	0.51138	−12.27	1811	21.375	15.788	41.875
APD/K/4	317	226	14.9	88.1	4.071	0.74779	0.719423	207.4773	0.1029	0.511592	0.511262	−14.56	1979	18.371	15.697	40.290
APD/K/5	347	136	6.96	43.5	7.411	0.77329	0.72165	239.0749	0.0976	0.511675	0.511362	−12.61	1782	20.026	15.772	40.543
APD/K/6	301	171	11.7	70.0	5.040	0.75131	0.716191	161.6203	0.1014	0.511720	0.511395	−11.97	1782	19.654	15.761	40.018
APD/K/7	274	277	21.7	130	2.872	0.74004	0.720028	216.0613	0.1016	0.511556	0.511231	−15.18	2008	18.518	15.698	40.582
APD/K/8	398	95.1	6.5	39.2	12.22	0.80671	0.721561	237.8121	0.1008	0.511776	0.511453	−10.84	1698	46.879	18.375	40.586
APD/K/9	409	95.1	7.05	42.9	12.57	0.80646	0.718873	199.6737	0.1002					59.758	19.926	40.936
%Error 2σ	2	1	1	1	2	0.05			1	0.005				0.2	0.2	0.2

Table 8. Rb-Sr, Sm-Nd, and Pb-Pb data on Dengaon granite.

Sample No.	Rb	Sr	Sm	Nd	$^{87}Rb/^{86}Sr$	$^{87}Sr/^{86}Sr$	$^{87}Sr/^{86}Sr$ (I)	εSr	$^{147}Sm/^{144}Nd$	$^{143}Nd/^{144}Nc$	$^{143}Nd/^{144}Nd$ (I)	εNd	Model Age (Ma (TDm)	$^{206}Pb/^{204}Pb$	$^{207}Pb/^{204}Pb$	$^{208}Pb/^{204}Pb$
MHKU-1	291	277	20	135	3.047	0.7394	0.715161	487.94	0.0903	0.511545	0.511215	−13.75	1838	19.152	15.647	39.895
MHKU-1A	284	285	20.9	138	2.885	0.7395	0.71655	489.36	0.092	0.511524	0.511188	−14.28	1889	20.304	15.808	40.032
MHKU-2	381	87.6	7.52	34.2	12.71	0.81605	0.714941	1575.18	0.1341	0.511857	0.511367	−10.79	2259	20.343	15.807	39.999
MHKU-3	485	104	7.51	40.3	13.69	0.81807	0.709165	1603.83	0.1134	0.51169	0.511275	−12.57	2043	19.715	15.787	40.399
MHKU-4	320	134	6.58	40.6	6.955	0.77068	0.715352	931.63	0.0986	0.51178	0.51142	−9.75	1660	20.053	15.784	40.562
MHKU-4A	349	137	9.21	41.4	7.44	0.77642	0.717234	1013.05	0.1355	0.511788	0.511293	−12.23	2439	19.988	15.782	40.642
%Errors 2σ	2	1	1	1	2	0.05			1	0.005				0.2	0.2	0.2

Analyst: Nayak *et al.* 2009

10. Discussions

The Kathalguri Granite shows negative Eu anomaly with Eu/Eu* between 0.269 to 0.709 and mantle normalized (La/Yb)N values between 8.18 to 19.17 are suggestive of Kathalguri Granites likely originated from partial melting of a garnet-bearing crustal source in a high-pressure environment, with significant plagioclase fractionation and possible crustal contamination. This scenario is consistent with granites formed in continental arc or post-collisional settings, where tectonic processes drive partial melting and crustal differentiation. The Kathalguri Granites exhibit significantly elevated Sr/Y ratios ranging from 0.82 to 37.82, with an average of 13.98. This suggests that their origin may be attributed to the melting of granitoids with high Sr/Y ratios, or by melts generated in continental crust lithologies. Mantle-derived melts are usually characterized by low Sr/Y values (~3) which may be increased during subduction-related enrichment episodes (Vellmer & Vedepohl, 1994; Moyen, 2009) [71] [72]. Both the signatures are observed for

Kathalguri Granites. Fractional crystallization was also confirmed by the high differentiation index (DI) ranging from 75.49 to 92.16 (**Table 1**) and the obvious fractionation between LREE and HREE. The Kathalguri Granites also show multiple source contributions in the melting process (**Figures 30(a)-(c)**).

Synthesis of available geochronological data on Assam Meghalaya Plateau (AMP) that they are in five phases modified after Dhurandhar *et al.* 2019 [3] (**Table 9**).

1. Phase I 2.2 to 2.0 Ga event represented by Rb-Sr isochron ages of intrusions of Porphyritic granites of Kanchanjuri, Bordekagaon, and Kuthori, Karbi hills Assam Majumdar and Dutta (2007) [73]. This stage correlates to the Kenorland, Lauroscandia supercontinent 2.7 to 2.1Ga (Lubnina and Slabunov, 2011; Mints and Eriksson, 2016) [74] [75] and also to the M_1, CD_{1a} of Chhotanagpur Granite Gneiss complex (CGGC) (Dhurandhar *et al.*, 2024) [76].
2. Phase II 1.9 to 1.5 Ga activities are evidenced by Rb-Sr isochron ages of Panbari porphyritic granite Karbi Hills 1953 ± 39 Ma Majumdar and Dutta (2007) [73], SHRIMP U-Pb zircon ages of granite gneisses of Rongjeng 1778 ± 37 Ma, Garo hills, Granite gneisses Pathrkang, Garo hills 1714 ± 44 Ma and. Karbi hills, Guwahati Granite gneiss (Monzogranite) 1630 ± 16 Ma, and Sonsak Porhyritic Syenogranite Garo Hills 1620.8 ± 9.2 Ma, and Longavalli granite gneiss A-1 1430.4 ± 9.6 Ma (Kumar *et al.*, 2017) [7], and LA-ICPMS U-Pb zircon ages of Panbari Geleki granite gneiss, Kaziranga Karbi Hills 1644 ± 33 Ma, Kuthori Porphyritic granite, Karbi Hills 1599 ± 17 Ma, Dalamara Porphyritic granite, Karbi Hills 1550 ± 25 Ma Gogoi *et al.* (2019) [6], Ion microprobe U-Pb zircon ages of Foliated biotite granite, Granite Gneiss, South of Guwahati 1598 ± 26, 1521 ± 28, 1100 Ma, Bramhaputra Augen Gniess 1520 Ma and 1630 Ma (Yin *et al.*, 2010) [77], Rhesu Granite gneiss, Garo Hills 1535 ± 110 to 1862 ± 63 Ma, and Ion microprobe Pb-Pb zircon Riangdo Granite gneiss West Khasi Hills 1415 ± 48 to 1451 ± 129 Ma Charnockite on Nongstoin Riangdo Road 7-G 1751 ± 70 Ma, 1481 ± 116 Ma (Bidyananda and Deomurari, 2007) [78]. Noritic Enclaves in South Khasi hills1462 ± 98 Ma (Ghose *et al.*, 1991: 94) [79] [80]. This stage correlates to the Pre-Rodinia Columbia (Nuna) supercontinent 1.9 - 1.75 Ga. Assembled during 1.6 Ga and fragmented during the interval 1.3 - 1.2 Ga (Zhang *et al.*, 2012; Meert and Santhosh, 2017) [81] [82].
3. Phase III 1.2 to 1.0 Ga events are presented by Rb-Sr isochrone ages of Mikir Hills Basic Dykes, 1200 ± 67 Ma Dhurandhar *et al.* 2019 [3], Karbi Hills, Granite Gneiss (S. Nongpoh) 1150 ± 26 Ma and Sindhuli Granite 881 ± 39 (Ghose *et al.* 1991: 94) [79] [80]. Ion probe U-Pb zircon age of Biotite-Granite AY03-05-(1)A, B, and C, Mikir Hills 500 to 1100 Ma (Yin *et al.*, 2010) [77]. The stage correlates to the Columbian supercontinent breakup cycle.
4. Phase IV 0.8 to 0.5 Ga activities are represented by Rb-Sr isochron ages of granite and granite gneisses from Rongjeng 788 ± 2 Ma, and south of Rongjeng 808 ± 32 Ma (Ghose *et al.*, 1991: 94) [79] [80], Songsak Garo 523 ± 7.9 Ma, and SHRIMP U-Pb zircon age for Kaziranga porphyritic granite KP-1 528.7 ± 5.5 Ma

Kumar *et al.* (2017) [7], and South Khasi batholiths 748 ± 26 Ma, 756 ± 60 Ma and 757 ± 19 Ma (Paneer Selvam *et al.*, 1995) [83] Mylliem 607 ± 13 Ma (Chimote *et al.*, 1988) [84], Rb Sr age for Nongpoh granite 550 ± 15 Ma Ghose *et al.*, 1991: 94) [79] [80]. Ion microprobe U-Pb zircon age for Nongpoh North Augen Gneiss 530 ± 7 & 490 ± 9 Ma Yin *et al.* (2010) [77], and Rb-Sr age Kyrdem Granites South Khasi hills of Meghalaya 479 ± 26 Ma (Ghose *et al.*, 1991: 94) [79] [80] and SHRIMP U-Pb zircon age of 512.5 ± 8.7 Ma by Kumar *et al.* (2017) [7]. Rb Sr isochrone age of Dengaon granite 558 ± 43 Ma (Nayak *et al.*, 2009) [85], and Rb-Sr isochrone age of Kathalguri Granite from Mikir hills Assam 489 ± 19 Ma (Present study). This also correlated LA-ICP MS Th-U-Pb age of 515.1 ± 3.3 Ma and Lu-Hf Zircon age of 515.5 ± 2.7 Ma (Majumdar and Dutta 2106) [5]. This stage correlates to the Rodinia supercontinent that existed from 1000 to 725 Ma. The Gondwana Assembly 520 - 450 Ma. the breakup of Rodinia that began about 725 Ma and subsequent amalgamation of Gondwanaland c. 620 - 580 Ma. Assembly of Gondwanaland lasted from c720 - 500 Ma (Nance and Murphy, 2018) [86]. The break out of Laurentia from Rodinia at c. 725 Ma marks the re-organization of lithospheric plate motion that resulted in the Pan-African-Brasiliano orogeny. (Wang *et al.*, 2012, 2020) [87] [88].

5. Phase V 0.17 to 0.1 Ma culminates at alkaline magmatism at Sung valley, Meghalaya K-Ar age of phlogopite separated from Sovite 149 ± 5 Ma (Sarkar *et al.* 1992) [89] to U-Pb age of 156 ± 16 Ma (Veena *et al.*, 1991) [90]. 134 ± 20 Ma Pb-Pb age of (Veena *et al.*, 1998) [91]. Sylhet trap near Umawai dated 130 ± 3 to 110 ± 3 Ma by K-Ar age (Sarkar, 1996) [92] from Sung Valley Pyroxenite and phlogopite are dated by K-A and Rb-Sr whole rock isochrone methods 106 - 107 Ma (Veena *et al.*, 1991, 1992; Ray *et al.*, 1999, 2000) [90] [91] [93] [94] Lamprophyre of Swangkre dated by Ar-Ar 114.9 ± 0.6 Ma (Coffine *et al.*, 2002) [95], and the whole rock dates of Swangkre Lamprophyre ranges from 107 ± 3, 107 ± 04 Ma (Sarkar *et al.*, 1992, 1996) [89] [92]. The alkaline magmatism at Jasra obtained by dating of Gabbro/zircon and baddeleyite by U-Pb ID-TIMS 105.2 ± 0.5 Ma (Heaman *et al.*, 2002) [96], Clinopyroxenite/perovskite of Jasra alkaline complex 101.6 ± 1.2 Ma by *in situ* U-Pb SIMS (Srivastava *et al.*, 2019) [97]. Barpung and Sampchampi area in Mikir hills are considered to be coeval of Sung valley magmatism of Meghalaya. The youngest one in this is by apatite from sung valley 80 ± 30 - 90 ± 10 Ma (Chattopadhyay and Hashimi, 1984) [98]. Ultramafic-mafic and alkaline magmatism area are considered as mantle plumes to be related to deep dynamic mechanism for development of Large Igneous Province (LIP). This particular phase (Rajmahal-Sylhet trap) can be related to Kerguelen mantle plum and Comei-Cona-Yamdrok areas of eastern Tethyan Himalaya with the Bunbury basalts in southwestern Australia (Zhu *et al.*, 2008, 2009) [99] [100]. The global synthesis shows the mafic-alkaline and carbonatite affinity to Continental Flood Basalt (CFB) magmatism like Parana CFB 133 - 129 Ma and associated Ponta Grossa Alkaline-carbonatite igneous complex (ACIC) 130 ± 5 Ma; Etendeka CFB 132 - 129 Ma (Renne *et al.*, 1992,

1996) [101] [102] and associated Angolia/Namibia ACIC 120 ± 2 Ma (Woolley and Kempe 1989) [103]; Deccan CFB 69 - 63 Ma (Duncan and Pyle, 1988; Venkatesan *et al.*, 1993) [104] [105] and associated Chhota Udepur ACIC (65 ± 0.2 Ma) (Ray and Pande, 1999) [93]. This stage also correlates well to the breakup of Gondwanaland ~140 - 130 Ma.

Table 9. Geochronological age data for the Assam Meghalaya Plateau.

Rock Type	Method	Age Ma	Initial Sr Ratio	Sources
Phase V 0.17 to 0.1 Ma				
Apatite from Sung Valley	Fission Track	80 ± 13 Ma 90 ± 10 Ma		Chattopadhyay and Hashimi 1984
Jasra, Clinopyroxenite/Perovskite	*In situ* U-Pb SIMS	101.6 ± 1.2 Ma		Srivastava *et al.* 2019
Samchampi-Samteran, Carbonatite/Apatite	Fission track	~105 Ma		Acharya *et al.* 1986
Sung Valley Pyroxenite and Phlogopite separated from Carbonatite. Carbonatite Age of Sung Valley	Ar-Ar	107.2 ± 0.8 Ma		Ray *et al.* 1999
	Rb-Sr	106 ± 11 Ma		Ray *et al.* 2000
	Rb-Sr	107.2 ± 0.8 Ma		Veena *et al.* 1991
		106 ± 11 Ma		Veena *et al.* 1991
Jasra Alkaline Complex, Gabbro/zircon and baddeleyite	U-Pb ID-TIMS	105.2 ± 0.5 Ma		Heaman *et al.* 2002
Swangkre, Lamprophyre	K-Ar WR	107 ± 4 Ma		Sarkar *et al.* 1996
Lamprophyre Swangkre Alkaline Complex, E. Garo Hills, Meghalaya	K-Ar	107 ± 3 Ma		Sarkar *et al.* 1992
Swangkre (?) Lamprophyre/biotite	Ar-Ar	114.9 ± 0.6 Ma		Coffin *et al.* 2002
Sylhet Trap near Umwai, Meghalaya	K-Ar	110 ± 3 Ma 133 ± 3 Ma		Sarkar *et al.* 1996
Sung Valley Alkaline Complex, Meghalaya	Pb-Pb	134 ± 20 Ma		Veena *et al.* 1998
Phlogopite separated from Sovite Sung Valley	K-Ar	149 ± 5 Ma		Sarkar *et al.* 1992
	U-Pb	156 ± 16 Ma		Veena *et al.* 1991
Phase IV 0.8 to 0.5 Ga				
Kyrdem Granite	Rb-Sr	479 ± 26 Ma	0.71482 ± 0.00072	Ghose *et al.* 1991: 94
Kyrdem granite C-1, Kyrdem Plateau	SHRIMP U-Pb zircon	512.5 ± 8.7 Ma		Kumar *et al.* (2017)
Kathalguri Granite, Mikir Hills	Rb-Sr	489 ± 19 Ma	0.7199 ± 0.0017	Present study
Bamuni Granite, Mikir Hills	HR-SIMS U-Pb zircon	490 ± 11 Ma		Hazarika *et al.* (2023)
Kathalguri Granite, Mikir Hills	LA-ICP MS Th-U-Pb	515.1 ± 3.3 Ma		Majumdar and Dutta 2016
	Lu-Hf Zircon	515.5 ± 2.7 Ma		

Continued

Kaziranga porphyritic granite KP-1	SHRIMP U-Pb zircon	528.7 ± 5.5 Ma		Kumar *et al.* (2017)
Songsak Granite	Rb-Sr	500 ± 40 Ma	0.728 ± 0.0003	Ghose *et al.* 1991: 94
Nongpoh granite F-4 Nongpoh Pluton	SHRIMP U-Pb zircon	506.7 ± 7.1 Ma 535 ± 11 Ma		Kumar *et al.* (2017)
Nongpoh North Augen Gneiss	Ion microprobe U-Pb zircon	530 ± 7 & 490 ± 9 Ma		Yin *et al.* (2010)
Nongpoh Granite	Rb-Sr	550 ± 15 Ma	0.70948 ± 0.00047	Ghose *et al.* 1991: 94
Sakwang granite D-6	SHRIMP U-Pb zircon	516 ± 9 Ma		Kumar *et al.* 2017
Dengaon Granite, Mikir Hills	Rb-Sr WR	558 ± 43 Ma	0.7159 ± 0.0029	Nayak *et al.* 2009
Mylliem Granite	Rb-Sr WR	607 ± 13 Ma	0.71187 ± 0.00047	Chimote *et al.* 1988
South Khasi Batholith (Pink)	Rb-Sr WR	748 ± 26 Ma	0.71074 ± 0.00043	Paneer Selvam *et al.* 1995
South Khasi Batholith (Grey)	Rb-Sr WR	756 ± 60 Ma	0.71069 ± 0.00092	
South Khasi Batholith (Porphyritic)	Rb-Sr WR	757 ± 19 Ma	0.71074 ± 0.00029	
Rongjeng Granite	Rb-Sr WR	788 ± 21 Ma	0.70699 ± 0.0002	Ghose *et al.* 1991: 94
Granite Gneiss (South Rongjeng)	Rb-Sr WR	808 ± 32 Ma	0.72594 ± 0.00064	
Phase III 1.2 to 1.0 Ga				
Sindhuli Granite	Rb-Sr WR	881 ± 39 Ma	0.70517 ± 0.00068	Ghose *et al.* 1991: 94
Biotite-Granite AY03-05-(1)A, B, and C, Mikir Hills	Ion microprobe U-Pb zircon	500 to 1100 Ma		Yin *et al.* 2010
Granite Gneiss (S. Nongpoh)	Rb-Sr	1150 ± 26 Ma	0.70681 ± 0.00049	Ghose *et al.* 1991: 94
Mikir Hills Basic Dykes	Rb-Sr	1200 ± 67 Ma	0.70477 ± 0.00042	Dhurandhar *et al.* 2019
Phase II 1.9 to 1.5 Ga				
Riangdo Granite gneiss West Khasi Hills	Ion microprobe Pb-Pb zircon	1415 ± 48 Ma to 1451 ± 129 Ma		Bidyananda and Deomurari 2007
Charnockite on Nongstoin Riangdo Raod 7-G	Ion microprobe Pb-Pb zircon	1751 ± 70 Ma 1481 ± 116 Ma		
Longavalli granite gneiss A-1	SHRIMP U-Pb zircon	1430.4 ± 9.6 Ma		Kumar *et al.* 2017
Noritic Enclave (SKB)	Rb-Sr	1462 ± 98 Ma	0.70459 ± 0.00076	Ghose *et al.* 1991: 94
Rhesu Granite gneiss, Garo Hills,	Ion microprobe Pb-Pb zircon	1535 ± 110 to 1862 ± 63		Bidyananda and Deomurari 2007
Dalamara Porphyritic granite, Karbi Hills	LA-ICPMS U-Pb zircon	1550 ± 25 Ma		Gogoi *et al.* 2019
Foliated biotite granite, Granite Gneiss, South of Guwahati	Ion microprobe U-Pb zircon	1598 ± 26, 1521 ± 28, 1100		Yin *et al.* (2010)
Bramhaputra Augen Gniess AY 02-07-06-(2)	Ion microprobe U-Pb zircon	1520 Ma and 1630 Ma		
Kuthori Porphyritic granite, Karbi Hills	LA-ICPMS U-Pb zircon	1599 ± 17 Ma		Gogoi *et al.* (2019)

Continued

Sonsak Granite gneiss (syenogranite), Garo Hills	SHIRMP U-Pb zircon	1620.8 ± 9.2 Ma 523 ± 7.9 Ma		Kumar *et al.* (2017)
Guwahati Granite gneiss (Monzogranite)	SHIRMP U-Pb zircon	1630 ± 16 Ma		
Panbari-Geleki Porphyritic granite, Kaziranga, Karbi Hills	LA-ICPMS U-Pb zircon	1644 ± 33 Ma		Gogoi *et al.* (2019)
Patharkang Granite Gneiss	Rb-Sr	1714 ± 44 Ma	0.70546 ± 0.00483	Ghose *et al.* 1991: 94
Rongjeng Granite gneiss (Monzogranite), Garo Hills, RJ-1	SHIRMP U-Pb zircon	1778 ± 37 Ma		Kumar *et al.* 2017
Panbari Porphyritic granite, Karbi Hills	Rb-Sr WR	1953 ± 39 Ma		Majumdar and Dutta (2007)
Phase I 2.2 Ga to 2.0 Ga				
Kuthori Porphyritic granite, Karbi Hills	Rb-Sr WR	2027 ± 41 Ma		
Bordekagaon Porphyritic granite, Karbi Hills	Rb-Sr WR	2046 ± 41 Ma		Majumdar and Dutta (2007)
Kanchanjuri Porphyritic granite, Karbi Hills	Rb-Sr WR	2152 ± 43 Ma		

11. Conclusion

Satellite image analysis revealed the lithostructural details of the area like broad lithologies, lineaments folds and faults, and follow-up geological mapping has confirmed the regional structures and folding in Barapani formation. Some major folds identified are Dongphlang anticline, Lalmati anticline, and a syncline in Rengbeng hillock. Three phases of folding (F1, F2 and F3) are also deciphered. The strain analysis of the stretched conglomerate suggests that the conglomerate has suffered initial pre-tectonic compaction; the initial tectonic deformation increments can give rise to apparent constrictive finite strains with the X-axis at right angles to the tectonic X-axis, with a certain value of initial compaction and superposed tectonic deformation. The stretched pebble belongs to LS tectonite, which is developed by the deformation related to the ancient tectonic deformations by Brahmaputra Rifting and the younger deformations induced by the intrusion of Kathalguri Granite. This dual fabric is common in areas subjected to transpressional tectonics, where both compressive and shear forces are at work. The presence of both transpressional and transtensional shears in the area also supports these events. Kathalguri Granite is metaluminous to peralkaline high silicious, potassic and ferruginous low magnesian within plate predominantly A2 type, some parts grading into A1 type granite. Kathalguri Granite formed under moderately oxidizing conditions and belongs to the magnetite series, with a pressure range of 5 - 15 kbars, and temperature 721˚C - 834˚C with an average of 815˚C and a depth of intrusion typically around 14 - 40 km deep. They exhibit elevated contents of LREE and depleted HREE, negative Eu anomaly, Eu/Eu* 0.27

to 0.71, radioelements and zircon. They are formed due to partial melting of crustal material and mixing with mantle-derived melts, which may have increased during subduction-related enrichment episodes. They also exhibit Fractional crystallization, confirmed by the high differentiation index (DI) ranging from 75.49 to 92.16 and the obvious fractionation between LREE and HREE, thus indicating multiple sources of melt generation. Kathalguri Granite are high heat-producing granite with HPU ranging between 4.34 to 15.27 Aμ·Wm^{-3} with an average of 10.65 Aμ·Wm^{-3}. Kathalguri Granite has given an isochron age of 489 ± 19 Ma with an initial $^{87}Sr/^{86}Sr$ 0.7199 ± 0.0017 and MSWD of 4.1. The Dengaon granite gave an isochron age of 558 ± 43 Ma with an initial $^{87}Sr/^{86}Sr$ 0.7159 ± 0.0029 and MSWD of 5.7. The mantle-depleted model ages of Kathalguri Granite (1661 - 2008 Ma), and Dengaon granite (1660 to 2439 Ma) both indicate that the protolith from which these granites are derived is mostly Meso- to Paleoproterozoic in age. Their intrusion relates to the Cambrian Pan African-Braziliano orogenic movement and crustal reorganization event. The review and synthesis of geochronological data suggested five phases of tectono-magmatic evolution of Assam Meghalaya Plateau viz. Phase I 2.2 to 2.0 Ga, Phase II 1.9 to 1.5 Ga, Phase III 1.2 to 1.0 Ga, Phase IV 0.8 to 0.5 Ga, and Phase V 0.17 to 0.1 Ma. The presence of xenoliths of older mafic rocks and Barapani arenites within the Kathalguri Granite, geochemical, and isotopic signatures of recycled crustal materials, both mafic and sedimentary, suggests some heterogeneity or multiple source contributions in the melting process. The AMP evolution ranges from Kenorland Lauroscandia, Columbia (Nuna), Rodinia, and Gondwanaland breakups and culminates at mafic-alkaline and carbonatite affinity to Continental Flood Basalt (CFB) related to Kerguelen mantle plume and Comei-Cona-Yamdrok areas of eastern Tethyan Himalaya.

Acknowledgements

The author acknowledges the analytical support from XRF, Laboratory Atomic Minerals Directorate for Exploration & Research (AMD) Nagpur, geochronology laboratory AMD Hyderabad, ICP-MS analysis of rare earth elements Shiva Analytical Bangalore, and AMD Shillong for providing logistics facilities during the field works. Assam State Electricity Board (ASEB) has also acknowledged providing accommodation at Kotputali during field investigations. The author is thankful to the Editor for inviting this paper and for the editorial handling of the manuscript. The author is also thankful to the anonymous reviewers for their valuable suggestions and comments for improving the manuscript.

Conflict of Interests

There are no conflicts of interests.

Data Availability

All the data discussed are included in the paper.

Copyrighted Material Used in the Manuscript

Not Applicable. All the data and materials used are generated and interpreted by the author.

References

[1] Nandi, D.R. (2001) Geodynamics of Northeast India and Adjoining Regions. ACB Publications.

[2] Mallikharjuna Rao, J., Poornachandra Rao, G.V.S. and Sarma, K.P. (2009) Precambrian Mafic Magmatism of Shillong Plateau, Meghalaya and Their Evolutionary History. *Journal of the Geological Society of India*, **73**, 143-152. https://doi.org/10.1007/s12594-009-0009-9

[3] Dhurandhar, A.P., Pandey, U.K. and Raminaidu, C. (2019) Petrochemistry and Sr, Nd, Pb Isotopic Characteristics of Basic Dykes of Mikir Hills, Assam. *Journal of the Geological Society of India*, **94**, 559-572. https://doi.org/10.1007/s12594-019-1361-z

[4] Prakash, T., Saikia, A., Basumatary, P. and Gogoi, B. (2023) Petrogenesis of the Borjuri Diorite Pluton in the Mikir Massif of Northeast India: Implications for Post-Collisional Intermediate Magmatism during the Pan-African Orogeny. *Acta Geochimica*, **42**, 747-764. https://doi.org/10.1007/s11631-023-00613-x

[5] Majumdar, D. and Dutta, P. (2016) Geodynamic Evolution of a Pan-African Granitoid of Extended Dizo Valley in Karbi Hills, NE India: Evidence from Geochemistry and Isotope Geology. *Journal of Asian Earth Sciences*, **117**, 256-268. https://doi.org/10.1016/j.jseaes.2015.12.015

[6] Gogoi, A., Majumdar, D., Cottle, J. and Dutta, P. (2019) Geochronology and Geochemistry of Mesoproterozoic Porphyry Granitoids in the Northern Karbi Hills, NE India: Implications for Early Tectonic Evolution of the Karbi Massif. *Journal of Asian Earth Sciences*, **179**, 65-79. https://doi.org/10.1016/j.jseaes.2019.04.013

[7] Kumar, S., Rino, V., Hayasaka, Y., Kimura, K., Raju, S., Terada, K., *et al.* (2017) Contribution of Columbia and Gondwana Supercontinent Assembly- and Growth-Related Magmatism in the Evolution of the Meghalaya Plateau and the Mikir Hills, Northeast India: Constraints from U-Pb SHRIMP Zircon Geochronology and Geochemistry. *Lithos*, **277**, 356-375. https://doi.org/10.1016/j.lithos.2016.10.020

[8] Hazarika, G. and Gogoi, B. (2022) Fractal Analysis and Geochemical Characterization of Mafic Magmatic Enclaves in the Kathalguri Pluton, Mikir Massif (Northeast India): Implications for Pan-African Bimodal Magmatism. *International Journal of Earth Sciences*, **112**, 685-705. https://doi.org/10.1007/s00531-022-02259-1

[9] Dhurandhar, A.P. (2005) Geological, Litho- and Hydrogeochemical Mapping of Parts of Mikir Hills Assam. Atomic Minerals Directorate, Hyderabad.

[10] Dhurandhar, A.P. (2010) Petrochemistry and Geochronology of Kathalguri Granite, Assam, India. Atomic Minerals Directorate, Hyderabad.

[11] Fry, N. (1979) Random Point Distributions and Strain Measurement in Rocks. *Tectonophysics*, **60**, 89-105. https://doi.org/10.1016/0040-1951(79)90135-5

[12] Ramsay, J.G. and Wood, D.S. (1973) The Geometric Effects of Volume Change during Deformation Processes. *Tectonophysics*, **16**, 263-277. https://doi.org/10.1016/0040-1951(73)90015-2

[13] Flinn, D. (1962) On Folding during Three-Dimensional Progressive Deformation. *Quarterly Journal of the Geological Society of London*, **118**, 385-428. https://doi.org/10.1144/gsjgs.118.1.0385

[14] Flinn, D. (1965) On the Symmetry Principle and the Deformation Ellipsoid. *Geological Magazine*, **102**, 36-45. https://doi.org/10.1017/s0016756800053851

[15] Flinn, D. (1978) Construction and Computation of Three-Dimensional Progressive Deformations. *Journal of the Geological Society*, **135**, 291-305. https://doi.org/10.1144/gsjgs.135.3.0291

[16] Hsu, T.C. (1966) The Characteristics of Coaxial and Non-Coaxial Strain Paths. *Journal of Strain Analysis*, **1**, 216-222. https://doi.org/10.1243/03093247v013216

[17] Burns, K.L. and Spry, A.H. (1969) Analysis of the Shape of Deformed Pebbles. *Tectonophysics*, **7**, 177-196. https://doi.org/10.1016/0040-1951(69)90066-3

[18] Ludwing, K.R. (2012) ISOPLOT 3.75 a Geochronological Toolkit for Microsoft Excel. Berkeley Geochronology Centre Special Publication.

[19] Pandey, B.K., Gupta, J.N., Sarma, K.J. and Sastry, C.A. (1997) Sm-Nd, Pb-Pb and Rb--Sr Geochronology and Petrogenesis of the Mafic Dyke Swarm of Mahbubnagar, South India: Implications for Paleoproterozoic Crustal Evolution of the Eastern Dharwar Craton. *Precambrian Research*, **84**, 181-196. https://doi.org/10.1016/s0301-9268(97)00027-2

[20] Streckeisen, A. (1976) To Each Plutonic Rock Its Proper Name. *Earth-Science Reviews*, **12**, 1-33. https://doi.org/10.1016/0012-8252(76)90052-0

[21] Enrique, P. (2018) Clasificación normativa de las rocas plutónicas saturadas y so-bresaturadas en sílice basada en la clasificación modal QAP: El diagrama 2Q-(or + ab)-4an. *Geogaceta*, **63**, 95-98. http://hdl.handle.net/10272/16739

[22] Wedepohl, K.H. (1969) Handbook of Geochemistry. Springer, 236.

[23] Gao, S., Luo, T., Zhang, B., Zhang, H., Han, Y., Zhao, Z., *et al.* (1998) Chemical Composition of the Continental Crust as Revealed by Studies in East China. *Geochimica et Cosmochimica Acta*, **62**, 1959-1975. https://doi.org/10.1016/s0016-7037(98)00121-5

[24] Thompson, R.N. (1982) Magmatism of the British Tertiary Volcanic Province. *Scottish Journal of Geology*, **18**, 49-107. https://doi.org/10.1144/sjg18010049

[25] Sun, S. and McDonough, W.F. (1989) Chemical and Isotopic Systematics of Oceanic Basalts: Implications for Mantle Composition and Processes. *Geological Society, London, Special Publications*, **42**, 313-345. https://doi.org/10.1144/gsl.sp.1989.042.01.19

[26] Blundy, J. and Cashman, K. (2008) Petrologic Reconstruction of Magmatic System Variables and Processes. *Reviews in Mineralogy and Geochemistry*, **69**, 179-239. https://doi.org/10.2138/rmg.2008.69.6

[27] Peccerillo, A. and Taylor, S.R. (1976) Geochemistry of Eocene Calc-Alkaline Volcanic Rocks from the Kastamonu Area, Northern Turkey. *Contributions to Mineralogy and Petrology*, **58**, 63-81. https://doi.org/10.1007/bf00384745

[28] Frost, B.R., Barnes, C.G., Collins, W.J., Arculus, R.J., Ellis, D.J. and Frost, C.D. (2001) A Geochemical Classification for Granitic Rocks. *Journal of Petrology*, **42**, 2033-2048. https://doi.org/10.1093/petrology/42.11.2033

[29] Maniar, P.D. and Piccoli, P.M. (1989) Tectonic Discrimination of Granitoids. *Geological Society of America Bulletin*, **101**, 635-643. https://doi.org/10.1130/0016-7606(1989)101<0635:tdog>2.3.co;2

[30] Taylor, S.R. (1965) The Application of Trace Element Data to Problems in Petrology. *Physics and Chemistry of the Earth*, **6**, 133-213. https://doi.org/10.1016/0079-1946(65)90014-5

[31] Rossi, J.N., Toselli, A.J., Basei, M.A., Sial, A.N. and Baez, M. (2011) Geochemical Indicators of Metalliferous Fertility in the Carboniferous San Blas Pluton, Sierra De Velasco, Argentina. *Geological Society*, *London*, *Special Publications*, **350**, 175-186. https://doi.org/10.1144/sp350.10

[32] Mason, B. (1966) Principals of Geochemistry. 3rd Edition, John Wiley & Sons, 610.

[33] Batchelor, R.A. and Bowden, P. (1985) Petrogenetic Interpretation of Granitoid Rock Series Using Multicationic Parameters. *Chemical Geology*, **48**, 43-55. https://doi.org/10.1016/0009-2541(85)90034-8

[34] Laurent, O., Martin, H., Moyen, J.F. and Doucelance, R. (2014) The Diversity and Evolution of Late-Archean Granitoids: Evidence for the Onset of "Modern-Style" Plate Tectonics between 3.0 and 2.5ga. *Lithos*, **205**, 208-235. https://doi.org/10.1016/j.lithos.2014.06.012

[35] Patiño Douce, A.E. (1999) What Do Experiments Tell Us about the Relative Contributions of Crust and Mantle to the Origin of Granitic Magmas? *Geological Society*, *London*, *Special Publications*, **168**, 55-75. https://doi.org/10.1144/gsl.sp.1999.168.01.05

[36] Jiang, Y., Jia, R., Liu, Z., Liao, S., Zhao, P. and Zhou, Q. (2013) Origin of Middle Triassic High-K Calc-Alkaline Granitoids and Their Potassic Microgranular Enclaves from the Western Kunlun Orogen, Northwest China: A Record of the Closure of Paleo-Tethys. *Lithos*, **156**, 13-30. https://doi.org/10.1016/j.lithos.2012.10.004

[37] Rapp, R.P., Watson, E.B. and Miller, C.F. (1991) Partial Melting of Amphibolite/eclogite and the Origin of Archean Trondhjemites and Tonalites. *Precambrian Research*, **51**, 1-25. https://doi.org/10.1016/0301-9268(91)90092-o

[38] Rapp, R.P. and Watson, E.B. (1995) Dehydration Melting of Metabasalt at 8-32 Kbar: Implications for Continental Growth and Crust-Mantle Recycling. *Journal of Petrology*, **36**, 891-931. https://doi.org/10.1093/petrology/36.4.891

[39] Sisson, T.W., Ratajeski, K., Hankins, W.B. and Glazner, A.F. (2004) Voluminous Granitic Magmas from Common Basaltic Sources. *Contributions to Mineralogy and Petrology*, **148**, 635-661. https://doi.org/10.1007/s00410-004-0632-9

[40] Whalen, J.B., Currie, K.L. and Chappell, B.W. (1987) A-type Granites: Geochemical Characteristics, Discrimination and Petrogenesis. *Contributions to Mineralogy and Petrology*, **95**, 407-419. https://doi.org/10.1007/bf00402202

[41] Eby, G.N. (1992) Chemical Subdivision of the A-Type Granitoids:petrogenetic and Tectonic Implications. *Geology*, **20**, 641-644. https://doi.org/10.1130/0091-7613(1992)020<0641:csotat>2.3.co;2

[42] Pearce, J.A. and Gale, G.H. (1977) Identification of Ore-Deposition Environment from Trace-Element Geochemistry of Associated Igneous Host Rocks. *Geological Society*, *London*, *Special Publications*, **7**, 14-24. https://doi.org/10.1144/gsl.sp.1977.007.01.03

[43] Mittlefehldt, D.W. and Miller, C.F. (1983) Geochemistry of the Sweetwater Wash Pluton, California: Implications for "Anomalous" Trace Element Behavior during Differentiation of Felsic Magmas. *Geochimica et Cosmochimica Acta*, **47**, 109-124. https://doi.org/10.1016/0016-7037(83)90095-9

[44] Philips, G.N., Wall, V.J. and Clemens, J.D. (1981) Petrology of the Strathbogie Batholith—A Cordierite Bearing Granite. *Canadian Mineralogist*, **19**, 47-63.

[45] Jackson, N.J., Walsh, J.N. and Pegram, E. (1984) Geology, Geochemistry and Petrogenesis of Late Precambrian Granitoids in the Central Hijaz Region of the Arabian Shield. *Contributions to Mineralogy and Petrology*, **87**, 205-219.

https://doi.org/10.1007/bf00373054

[46] Clemens, J.D., Holloway, J.R. and White, A.J.R. (1986) Origin of an A-Type Granite; Experimental Constraints. *American Mineralogist*, **71**, 317-324.

[47] BONIN, B. (2007) A-type Granites and Related Rocks: Evolution of a Concept, Problems and Prospects. *Lithos*, **97**, 1-29. https://doi.org/10.1016/j.lithos.2006.12.007

[48] Eby, G.N. (1990) The A-Type Granitoids: A Review of Their Occurrence and Chemical Characteristics and Speculations on Their Petrogenesis. *Lithos*, **26**, 115-134. https://doi.org/10.1016/0024-4937(90)90043-z

[49] Mushkin, A. (2003) The Petrogenesis of A-Type Magmas from the Amram Massif, Southern Israel. *Journal of Petrology*, **44**, 815-832. https://doi.org/10.1093/petrology/44.5.815

[50] Litvinovsky, B.A., Jahn, B., Zanvilevich, A.N., Saunders, A., Poulain, S., Kuzmin, D.V., *et al.* (2002) Petrogenesis of Syenite-Granite Suites from the Bryansky Complex (Transbaikalia, Russia): Implications for the Origin of A-Type Granitoid Magmas. *Chemical Geology*, **189**, 105-133. https://doi.org/10.1016/s0009-2541(02)00142-0

[51] Anderson, J.L. (1983) Proterozoic Anorogenic Granite Plutonism of North America. In: Medaris Jr., L.G., Byers, C.W., Mickelson, D.M. and Shanks, W.C., Eds., *Geological Society of America Memoirs*, Geological Society of America, 133-154. https://doi.org/10.1130/mem161-p133

[52] Yang, J., Wu, F., Chung, S., Wilde, S.A. and Chu, M. (2006) A Hybrid Origin for the Qianshan A-Type Granite, Northeast China: Geochemical and Sr-Nd-Hf Isotopic Evidence. *Lithos*, **89**, 89-106. https://doi.org/10.1016/j.lithos.2005.10.002

[53] King, P.L., White, A.J.R., Chappell, B.W. and Allen, C.M. (1997) Characterization and Origin of Aluminous A-Type Granites from the Lachlan Fold Belt, Southeastern Australia. *Journal of Petrology*, **38**, 371-391. https://doi.org/10.1093/petroj/38.3.371

[54] Droop, G.T.R. (2003) Processes and Conditions during Contact Anatexis, Melt Escape and Restite Formation: The Huntly Gabbro Complex, NE Scotland. *Journal of Petrology*, **44**, 995-1029. https://doi.org/10.1093/petrology/44.6.995

[55] El Bouseily, A.M. and El Sokkary, A.A. (1975) The Relation between Rb, Ba and Sr in Granitic Rocks. *Chemical Geology*, **16**, 207-219. https://doi.org/10.1016/0009-2541(75)90029-7

[56] Ishihara, S. (1977) The Magnetite Series and Ilmenite Series of Granitic Rocks. *Mining Geology*, **27**, 293-305. https://doi.org/10.11456/SHIGENCHISHITSU1951.27.293

[57] Blevin, P.L. (2004) Redox and Compositional Parameters for Interpreting the Granitoid Metallogeny of Eastern Australia: Implications for Gold-Rich Ore Systems. *Resource Geology*, **54**, 241-252. https://doi.org/10.1111/j.1751-3928.2004.tb00205.x

[58] Sylvester, P.J. (1998) Post-Collisional Strongly Peraluminous Granites. *Lithos*, **45**, 29-44. https://doi.org/10.1016/s0024-4937(98)00024-3

[59] Wu, F.Y., Lu, X.Y., Ji, W.Q., Wang, J.M. and Yang, L. (2017) Identification and Study of Highly Differentiated Granites. *Science China Press*, **47**, 745-765. (In Chinese)

[60] Schiano, P., Monzier, M., Eissen, J., Martin, H. and Koga, K.T. (2009) Simple Mixing as the Major Control of the Evolution of Volcanic Suites in the Ecuadorian Andes. *Contributions to Mineralogy and Petrology*, **160**, 297-312. https://doi.org/10.1007/s00410-009-0478-2

[61] Patiño Douce, A.E. and Johnston, A.D. (1991) Phase Equilibria and Melt Productivity in the Pelitic System: Implications for the Origin of Peraluminous Granitoids and Aluminous Granulites. *Contributions to Mineralogy and Petrology*, **107**, 202-218.

https://doi.org/10.1007/bf00310707

[62] Medaris Jr., L.G., Singer, B.S., Dott Jr., R.H., Naymark, A., Johnson, C.M. and Schott, R.C. (2003) Late Paleoproterozoic Climate, Tectonics, and Metamorphism in the Southern Lake Superior Region and Proto-North America: Evidence from Baraboo Interval Quartzites. *The Journal of Geology*, **111**, 243-257. https://doi.org/10.1086/373967

[63] Watson, E.B. and Harrison, T.M. (1983) Zircon Saturation Revisited: Temperature and Composition Effects in a Variety of Crustal Magma Types. *Earth and Planetary Science Letters*, **64**, 295-304. https://doi.org/10.1016/0012-821x(83)90211-x

[64] Boehnke, P., Watson, E.B., Trail, D., Harrison, T.M. and Schmitt, A.K. (2013) Zircon saturation Re-revisited. *Chemical Geology*, **351**, 324-334. https://doi.org/10.1016/j.chemgeo.2013.05.028

[65] Ryerson, F.J. and Watson, E.B. (1987) Rutile Saturation in Magmas: Implications for Tinbta Depletion in Island-Arc Basalts. *Earth and Planetary Science Letters*, **86**, 225-239. https://doi.org/10.1016/0012-821x(87)90223-8

[66] Hayden, L.A. and Watson, E.B. (2007) Rutile Saturation in Hydrous Siliceous Melts and Its Bearing on Ti-Thermometry of Quartz and Zircon. *Earth and Planetary Science Letters*, **258**, 561-568. https://doi.org/10.1016/j.epsl.2007.04.020

[67] Yang, X. (2017) Estimation of Crystallization Pressure of Granite Intrusions. *Lithos*, **286**, 324-329. https://doi.org/10.1016/j.lithos.2017.06.018

[68] Defant, M.J., Jackson, T.E., Drummond, M.S., De Boer, J.Z., Bellon, H., Feigenson, M.D., *et al*. (1992) The Geochemistry of Young Volcanism Throughout Western Panama and Southeastern Costa Rica: An Overview. *Journal of the Geological Society*, **149**, 569-579. https://doi.org/10.1144/gsjgs.149.4.0569

[69] Zartman, R.E. and Doe, B.R. (1981) Plumbotectonics—The Model. *Tectonophysics*, **75**, 135-162. https://doi.org/10.1016/0040-1951(81)90213-4

[70] Liu, S., Hu, R., Feng, C., Gao, S., Feng, G., Qi, Y., *et al*. (2012) U-Pb Zircon Age, Geochemical and Sr-Nd Isotopic Constraints on the Age and Origin of the Granodiorites in Guilong, Southeastern Yunnan Province, Southern China. *Open Journal of Geology*, **2**, 229-240. https://doi.org/10.4236/ojg.2012.24023

[71] Vellmer, C. and Wedepohl, K.H. (1994) Geochemical Characterization and Origin of Granitoids from the South Bohemian Batholith in Lower Austria. *Contributions to Mineralogy and Petrology*, **118**, 13-32. https://doi.org/10.1007/bf00310608

[72] Moyen, J. (2009) High Sr/Y and La/Yb Ratios: The Meaning of the "Adakitic Signature". *Lithos*, **112**, 556-574. https://doi.org/10.1016/j.lithos.2009.04.001

[73] Majumdar, D. and Dutta, S. (2007) Geological Investigations on Sulphide Ore Occurrences in Magmatic Complex, Mikir Hills, Assam. *Indian Geological Congress. Bull*, **1**, 7-21.

[74] Lubnina, N.V. and Slabunov, A.I. (2011) Reconstruction of the Kenorland Supercontinent in the Neoarchean Based on Paleomagnetic and Geological Data. *Moscow University Geology Bulletin*, **66**, 242-249. https://doi.org/10.3103/s0145875211040077

[75] Mints, M.V. and Eriksson, P.G. (2016) Secular Changes in Relationships between Plate-Tectonic and Mantle-Plume Engendered Processes during Precambrian Time. *Geodynamics & Tectonophysics*, **7**, 173-232. https://doi.org/10.5800/gt-2016-7-2-0203

[76] Dhurandhar, A.P., Rajagopalan, V. and Paul, A.K. (2024) Mineral Chemistry and Petrochronology of Zircon from Paleo-Mesoproterozoic Dudhi Group, Northwestern Chhotanagpur Granite Gneiss Complex, India.

[77] Yin, A., Dubey, C.S., Webb, A.A.G., Kelty, T.K., Grove, M., Gehrels, G.E., *et al.* (2009) Geologic Correlation of the Himalayan Orogen and Indian Craton: Part 1. Structural Geology, U-Pb Zircon Geochronology, and Tectonic Evolution of the Shillong Plateau and Its Neighboring Regions in NE India. *Geological Society of America Bulletin*, **122**, 336-359. https://doi.org/10.1130/b26460.1

[78] Bidyanand, M. and Deomurari, M.P. (2007) Geochronological Constraints on the Evolution of Meghalaya Massif, Northeastern India: An Ion Microprobe Study. *Current Science*, **93**, 1620-1623.

[79] Ghosh, S., Chakraborty, S., Bhalla, J.K., Paul, D.K., Sarkari, A., Bishui, P.K., *et al.* (1991) Geochronology and Geochemistry of Granite Plutons from East Khasi Hills, Meghalaya. *Journal Geological Society of India*, **37**, 331-342. https://doi.org/10.17491/jgsi/1991/370403

[80] Ghose, S., Chakraborty, S., Paul, D.K., Bhalla, J.K., Bishui, P.K. and Gupta, S.N. (1994) A New Rb-Sr Ages and Geochemistry of Granitoids from Meghalaya and Their Significance in Middle to Late Proterozoic Crustal Evolution. *Indian Minerals*, **48**, 33-44.

[81] Zhang, S., Li, Z., Evans, D.A.D., Wu, H., Li, H. and Dong, J. (2012) Pre-Rodinia Supercontinent Nuna Shaping Up: A Global Synthesis with New Paleomagnetic Results from North China. *Earth and Planetary Science Letters*, **353**, 145-155. https://doi.org/10.1016/j.epsl.2012.07.034

[82] Meert, J.G. and Santosh, M. (2022) The Columbia Supercontinent: Retrospective, Status, and a Statistical Assessment of Paleomagnetic Poles Used in Reconstructions. *Gondwana Research*, **110**, 143-164. https://doi.org/10.1016/j.gr.2022.06.014

[83] Panneer Selvam, A., Prasad, R.N., Dhana Raju, R. and Sinha, R.M. (1995) Rb-Sr Age of the Metaluminous Granitoids of South Khasi Batholith, Meghalaya: Implications on Its Genesis and Pan-African Activity in Northeastern India. *Journal Geological Society of India*, **46**, 619-624. https://doi.org/10.17491/jgsi/1995/460606

[84] Chimote J.S., Pandey B.K., Bagchi A.K., Basu A.N. and Saraswat A.C. (1988) Rb-Sr Whole Rock Isochron Age for the Mylliem Granite. *Proceedings* 4*th National Symposium on Mass Spectrometry*, Bangalore, 4-6 January 1988, 9/1-9/4.

[85] Nayak, S.K., Asha, K. and Rupa, N. (2009) Geochronology Report on Dengaon Granite. AMD.

[86] Nance, R.D. and Murphy, J.B. (2018) Supercontinents and the Case for Pannotia. *Geological Society, London, Special Publications*, **470**, 65-86. https://doi.org/10.1144/sp470.5

[87] Wang, X., Zhang, J., Santosh, M., Liu, J., Yan, S. and Guo, L. (2012) Andean-Type Orogeny in the Himalayas of South Tibet: Implications for Early Paleozoic Tectonics along the Indian Margin of Gondwana. *Lithos*, **154**, 248-262. https://doi.org/10.1016/j.lithos.2012.07.011

[88] Wang, H., Zhai, Q., Hu, P., Zeng, L., Tang, Y. and Zhu, Z. (2020) Late Cambrian to Early Silurian Granitic Rocks of the Gemuri Area, Central Qiangtang, North Tibet: New Constraints on the Tectonic Evolution of the Northern Margin of Gondwana. *Acta Geologica Sinica—English Edition*, **94**, 1007-1019. https://doi.org/10.1111/1755-6724.14556

[89] Sarkar, A., Datta, A.K., Poddar, B.C., Kollapuri, V.K., Bhattacharyya, B.K. and Sanwal, R. (1992) Geochronological Studies on Early Cretaceous Effusive and Intrusive Rocks from Northeast India. In: Ghose, N.C., Eds., *Mesozoic Magmatism of the Eastern Margin of India*, Patna University, 28-29.

[90] Veena Krishna, P.B.K., Krishnamurthy, P. and Gupta, J.N. (1991) Pb, Sr, and Nd Iso-

tope Systematics of Sung Valley Carbonatites. Meghalaya, India: Implications for Contemporary Sub-Crustal Upper Mantle Characterisation. *Proceeding of 5th National Symposium Mass Spectrometry*, Physical Research Laboratory, Ahmadabad, 7-9 January 1991, Abstract volume.

[91] Veena, K., Pandey, B.K., Krishnamurthy, P. and Gupta, J.N. (1998) Pb, Sr and Nd Isotopic Systematics of the Carbonatites of Sung Valley, Meghalaya, Northeast India: Implications for Contemporary Plume-Related Mantle Source Characteristics. *Journal of Petrology*, **39**, 1875-1884. https://doi.org/10.1093/petroj/39.11-12.1875

[92] Sarkar, A., Datta, A.K., Poddar, B.C., Bhattacharyya, B.K., Kollapuri, V.K. and Sanwal, R. (1996) Geochronological Studies of Mesozoic Igneous Rocks from Eastern India. *Journal of Southeast Asian Earth Sciences*, **13**, 77-81. https://doi.org/10.1016/0743-9547(96)00009-8

[93] Ray, J.S., Ramesh, R. and Pande, K. (1999) Carbon Isotopes in Kerguelen Plume-Derived Carbonatites: Evidence for Recycled Inorganic Carbon. *Earth and Planetary Science Letters*, **170**, 205-214. https://doi.org/10.1016/s0012-821x(99)00112-0

[94] Ray, J.S., Trivedi, J.R. and Dayal, A.M. (2000) Strontium Isotope Systematics of Amba Dongar and Sung Valley Carbonatite-Alkaline Complexes, India: Evidence for Liquid Immiscibility, Crustal Contamination and Long-Lived Rb/Sr Enriched Mantle Sources. *Journal of Asian Earth Sciences*, **18**, 585-594. https://doi.org/10.1016/s1367-9120(99)00072-3

[95] Coffin, M.F. (2002) Kerguelen Hotspot Magma Output since 130 Ma. *Journal of Petrology*, **43**, 1121-1137. https://doi.org/10.1093/petrology/43.7.1121

[96] Heaman, L.M., Srivastava, R.K. and Sinha, A.K. (2002) A Precise U-Pb Zircon/Baddeleyite Age for the Jasra Igneous Complex, Karb-Analong District, Assam, NE India. *Current Science*, **82**, 744-748.

[97] Srivastava, R.K., Guarino, V., Wu, F., Melluso, L. and Sinha, A.K. (2019) Evidence of Sub-Continental Lithospheric Mantle Sources and Open-System Crystallization Processes from *In-Situ* U-Pb Ages and Nd-Sr-Hf Isotope Geochemistry of the Cretaceous Ultramafic-Alkaline-(Carbonatite) Intrusions from the Shillong Plateau, North-Eastern India. *Lithos*, **330**, 108-119. https://doi.org/10.1016/j.lithos.2019.02.009

[98] Chattopadhyay, N. and Hashimi, S. (1984) The Sung Valley Alkaline Ultramafic Carbonatite Complex, East Khasi and Jaintia Hills Districts, Meghalaya. *Records of the Geological Survey of India*, **113**, 24-33.

[99] Zhu, D., Mo, X., Pan, G., Zhao, Z., Dong, G., Shi, Y., *et al.* (2008) Petrogenesis of the Earliest Early Cretaceous Mafic Rocks from the Cona Area of the Eastern Tethyan Himalaya in South Tibet: Interaction between the Incubating Kerguelen Plume and the Eastern Greater India Lithosphere? *Lithos*, **100**, 147-173. https://doi.org/10.1016/j.lithos.2007.06.024

[100] Zhu, D., Chung, S., Mo, X., Zhao, Z., Niu, Y., Song, B., *et al.* (2009) The 132 Ma Comei-Bunbury Large Igneous Province: Remnants Identified in Present-Day Southeastern Tibet and Southwestern Australia. *Geology*, **37**, 583-586. https://doi.org/10.1130/g30001a.1

[101] Renne, P.R., Ernesto, M., Pacca, I.G., Coe, R.S., Glen, J.M., Prévot, M., *et al.* (1992) The Age of Paraná Flood Volcanism, Rifting of Gondwanaland, and the Jurassic-Cretaceous Boundary. *Science*, **258**, 975-979. https://doi.org/10.1126/science.258.5084.975

[102] Renne, P.R., Deckart, K., Ernesto, M., Feraud, G. and Piccirillo, E.M. (1996) Age of the Ponta Grossa Dike Swarm (Brazil), and Implications to Parana Flood Volcanism. *Earth and Planetary Science Letters*, **144**, 199-211.

https://doi.org/10.1016/0012-821x(96)00155-0

[103] Woolley, A.R. and Kempe, D.R.C. (1989) Carbonatites: Nomenclature, Average Chemical Compositions, and Element Distribution. In: Bell, K., Ed., *Carbonatites, Genesis and Evolution*, Unwin Hyman, 1-14.

[104] Duncan, R.A. and Pyle, D.G. (1988) Rapid Eruption of the Deccan Flood Basalts at the Cretaceous/Tertiary Boundary. *Nature*, **333**, 841-843. https://doi.org/10.1038/333841a0

[105] Venkatesan, T.R., Pande, K. and Gopalan, K. (1993) Did Deccan Volcanism Pre-Date the Cretaceous/tertiary Transition? *Earth and Planetary Science Letters*, **119**, 181-189. https://doi.org/10.1016/0012-821x(93)90015-2